Acta Mech 233, 2989–3019 (2022)
https://doi.org/10.1007/s00707-022-03235-1

ORIGINAL PAPER

Raphael Scharf · Bernhard Pichler · Roman Heissenberger · Bernd Moritz · Christian Hellmich

Data-driven analytical mechanics of aging viscoelastic shotcrete tunnel shells

Received: 29 March 2022 / Accepted: 27 April 2022 / Published online: 2 July 2022

Abstract Based on the principle of virtual power, equilibrium conditions are established for the forces within a cross section of a tunnel top heading driven according the New Austrian Tunneling Method (NATM). External forces, namely impost actions and ground pressure distributions following a third-order polynomial, are analytically linked with internal forces, such as axial forces and bending moments, arising as integrals over the shell thickness, of circumferential normal stresses. The latter are related, via an aging viscoelastic shotcrete material model, to circumferential normal strains, as well as to radial and circumferential displacement components. This allows for analytical transformation of displacement measurement data collected at the crown and the footings of the shell segment, into ground pressure and impost action evolutions, together with all the associated force and stress quantities. For the Sieberg tunnel, driven in Miocene clay marl, our data-driven analytical mechanics model evidences virtually uniform ground pressure distributions, leading to a first rapidly increasing, and then mildly decreasing utilization degree of the shotcrete shell.

List of symbols

a/c	(Initial) aggregate-to-cement mass ratio
A	Cross-sectional area
A_i	Cubic shape functions (with $i = 1, 2, 3, 4$)
c_{hyd}	Cohesion of hydrates
C	Cross-sectional contour
C_i	Constants for the uniaxial compressive strength of the cement paste and shotcrete (with $i = 1, 2, 3, 4$)
$\hat{\mathbf{d}}$	Virtual Eulerian strain rate tensor
$\hat{d}_{ij}$	ij-th Component of the virtual Eulerian strain rate tensor
$\mathbf{e}_r, \mathbf{e}_\varphi, \mathbf{e}_z$	Unit base vectors of moving arch-like (cylindrical) coordinate system
$\mathbf{e}_x, \mathbf{e}_y, \mathbf{e}_z$	Unit base vectors of fixed Cartesian coordinate system
E	Young's modulus
$E_{28\text{d}}$	28-day value of Young's modulus of shotcrete
E_c	Creep modulus

R. Scharf · B. Pichler · C. Hellmich (✉)
Institute for Mechanics of Materials and Structures, TU Wien—Vienna University of Technology, Karlsplatz 13/202, 1040 Wien, Austria
E-mail: Christian.Hellmich@tuwien.ac.at

R. Heissenberger · B. Moritz
ÖBB—Infrastruktur AG, Streckenmanagement und Anlagenentwicklung, Fachbereich Bautechnik—Tunnelbau, Europaplatz 2/1, 8020 Graz, Austria

$E_{c,28\mathrm{d}}$	28-day value of creep modulus of shotcrete
$\mathbf{f}$	Volume forces
$f_{\mathrm{agg}}^{\mathrm{con}}$	Shotcrete-related aggregate volume fraction
f_b	Biaxial compressive strength of shotcrete
f_c	Uniaxial compressive strength of shotcrete
$f_{c,28\mathrm{d}}$	Uniaxial compressive strength of shotcrete reached 28 days after production
$f_{\mathrm{clin}}^{\mathrm{cp}}$	Cement paste-related clinker volume fraction
$f_{\mathrm{hyd}}^{\mathrm{hf}}$	Hydrate foam-related hydrate volume fraction
G_p	Ground pressure
$G_{p,i}$	Ground pressure at a specific point (with $i = 1, 2, 3, 4$)
h	Thickness of the tunnel shell segment
J	Creep function
J^{NL}	Nonlinear creep function
k_{DP}	Strength-like quantity in Drucker-Prager failure criterion
m_φ	Bending moments (per length)
$\mathbf{n}$	Outward normal onto a surface element dC
n_φ	Circumferential normal force (per length)
n_z	Longitudinal normal force (per length)
N_p	Impost forces
$N_{p,b}$, $N_{p,e}$	Axial forces at the beginning and at the end of the tunnel segment
p	Complex variable in Laplace-Carson domain
$\mathbf{r}$	Location vectors
r	Radial polar coordinate
R	Radius of the undeformed midsurface of a tunnel shell segment
$R_{\mathrm{ax}}^{\mathrm{shell}}$	Relaxation function in axial direction
$R_{\mathrm{lat}}^{\mathrm{shell}}$	Relaxation function in lateral direction
s	Arc length of the tunnel shell segment
s_E	Dimensionless strength and Young's modulus evolution parameter
s_{E_c}	Dimensionless creep modulus evolution parameter
t	Time variable
t_0	Reference time
$\mathbf{T}$	Traction forces
T_r	Radial component of the traction vector acting onto the outer surface of the tunnel shell
T_φ	Circumferential component of the traction vector acting onto the cross section at the beginning and end of the tunnel shell
u_r^C, u_φ^C	Radial and circumferential displacements of the gravitational center of the cross section
$u_{r,b}^C$, $u_{\varphi,b}^C$	Radial and circumferential displacements of the center surface at the beginning of the tunnel shell segment
$\hat{\mathbf{v}}$	Virtual velocity field
$\hat{v}_r$, $\hat{v}_\varphi$, $\hat{v}_z$	Radial, circumferential and longitudinal component of the virtual velocity
$\hat{v}_r^C$, $\hat{v}_\varphi^C$	Radial and circumferential component of the virtual velocity of the gravitational center of the cross section
w/c	(Initial) water-to-cement mass ratio
$(w/c)_{eff}$	Effective water-to-cement mass ratio
$\mathbf{x}$	Position vector
z	Longitudinal coordinate
α	Dimensionless parameter for the stiffness of the aggregates
α_{DP}	Dimensionless parameter of Drucker–Prager failure criterion
β	Power-law exponent
Γ	Gamma function
$\Delta\varphi$	Opening angle of the tunnel shell
Δt	Time increment
ε_{ii}	Normal strain in $\mathbf{e}_i$-direction (with $i = \varphi, r, z$)
η	Affinity factor

θ_z^C	Rotational angle of the shell generator line, around an axis oriented in $\mathbf{e}_z$-direction and positioned in the shell center
$\theta_{z,b}^C$, $\theta_{z,e}^C$	Rotational angle of the shell generator line, around an axis oriented in $\mathbf{e}_z$-direction and positioned in the shell center, at the beginning and at the end of the tunnel shell segment
κ	Ratio of biaxial to uniaxial compressive strength of shotcrete
ν	Poisson's ratio
ξ	Hydration degree of shotcrete
ρ_i	Mass densities of aggregates, clinker, and water (with $i = \text{agg, clin, } H_2O$)
$\boldsymbol{\sigma}$	Symmetric second-order Cauchy stress tensor
σ_{ii}	Normal stress in $\mathbf{e}_i$-direction (with $i = \varphi, r, z$)
$\Sigma_i^{\text{uni, ult}}$	Uniaxial compressive strength of the hydrate phase, hydrate foam, cement paste, and concrete (with $i = hyd, hf, cp, con$)
τ	Time instant of load application
φ	Circumferential polar coordinate
$\bar{\varphi}$	Circumferential polar coordinate starting from the beginning of the tunnel section
$\bar{\varphi}^*$	Position of maximum degree of utilization
φ_b, φ_e	Polar angle at the beginning and at the end of the tunnel segment
φ_{hyd}	Angle of internal friction of hydrates
$\hat{\omega}_z^C$	Virtual angular velocity component
$\mathcal{I}$	Time-invariant influence functions
$\mathcal{L}$	Level of loading associated with the strength of the material
$\mathcal{P}^{\text{int}}$	Virtual power of internal forces
$\mathcal{P}^{\text{ext}}$	Virtual power of external forces
$\times$	Exterior product (cross-product) of two vectors in 3D Euclidean space
$\cdot$	Inner product of two vectors in 3D Euclidean space
:	Second-order tensor contraction
$\otimes$	Dyadic product of two vectors
∇	Nabla operator
∂	Symbol used to denote partial derivatives
d	Symbol used for differentials

1 Introduction

As a rule, engineering structures are designed for *a priori* known, standardized external loads they have to withstand. This design strategy is heavily challenged in tunnel engineering where the loads acting on the tunnel shells are not known *a priori*: Since these loads are tightly linked to the interplay of the tunnel shell and the surrounding soil or rock, they heavily depend on geological details which remain unknown until the very construction phase. During the latter, the aforementioned interplay is standardly monitored in terms of displacement measurements, traditionally in terms of convergences [5,23]; and more recently in terms of laser-optical geodesy [29,30]. Hence, as a rule, both the loads acting on the tunnel shell and the stress states in the latter, need to be estimated from the aforementioned displacement measurements. This is very often done in the context of the so-called convergence-confinement method [3,5,22,24,31,32]. It reduces the ground-shell interactions to a plane-strain axisymmetric problem, with the tunnel radius change ("convergence") and the radial pressure acting at the shell-ground interface ("ground pressure") as the key physical properties. While this problem is particularly helpful for closed circular tunnel shells, its use for the construction phase where only part of the tunnel shell is installed, and where, consequently, the "ring closure" is not realized yet, is more questionable; and extensions for non-symmetric cases are desirable.

This is the very focus of the present contribution, dealing with (non-closed) top headings made of hydrating shotcrete in the framework of the New Austrian Tunneling Method (NATM), and monitored by means of geodetic displacement measurements of selected points on the inner surface of the tunnel shell. Rather than coming up with a mechanical model for the ground around the tunnel, we will explicitly incorporate the latter measurements into a "hybrid analysis" in the line of [2,11,12,19]. In this context, we will explicitly introduce the outer surface of the tunnel shell onto which normal traction forces ("ground pressure") will be imposed. Equilibrium of forces within each cross-sectional plane of the tunnel shell will be maintained by normal tractions acting on the footings of the tunnel shell segments.

The corresponding extension of the convergence-confinement methods is developed on the basis of key theoretical ingredients of continuum mechanics: (i) the principle of virtual power [6–10,35,40] applied to thin cylindrical shell segments (with the virtual motions being restricted to the cross-sectional plane of the tunnel shell), and (ii) multiscale aging viscoelasticity [28] quantifying the constitutive behavior of shotcrete.

Accordingly, the paper is organized as follows: We first recall the principle of virtual power, so as to develop an analytical circular arch theory governing the equilibrium of forces within the cross-sectional planes (Sect. 2). Thereafter, we transform power-law creep functions associated with uniaxial stress experiments, into shell-specific relaxation functions considering free inner shell surfaces and plane strain conditions (Sect. 3). Corresponding mathematical relationships are then combined in order to come up with elaborate analytical formulae linking displacement measurements at three geodetic laser-optical targets, with traction forces acting on a circular NATM tunnel heading (Sect. 4). These analytical tools are applied to the measurements performed at the Sieberg tunnel - a benchmark example having undergone various assessment strategies [12,37], before the results are discussed, so as to conclude the paper (Sect. 5).

2 Cross-sectional equilibrium within an arch-like tunnel cross section, derived from the principle of virtual power

2.1 Starting point—equilibrium of forces within tunnel cross section

According to the principle of virtual power [6–10,35] a mechanical system is in equilibrium (i.e., it fulfills the momentum and angular momentum conservation laws for the special case of negligibly small accelerations), if the power performed by the external and internal forces on an *arbitrary* virtual velocity field vanishes. We note that a mathematically identical principle is sometimes called principle of (rates of) virtual work; then the virtual velocities are called virtual motions [26,27].

We specify the principle of virtual power for the forces being equilibrated within a particular cross section of the tunnel, with a cross-sectional area A and a contour (boundary) C, see Fig. 1. All positions within such a cross section are labeled by vectors $\mathbf{x}$, and any continuous and differentiable velocity field $\hat{\mathbf{v}}(\mathbf{x})$ with vectors lying within the cross-sectional plane qualifies as admissible virtual velocity field. Then, the power density of external forces, per unit length measured along the tunnel axis, reads as

$$\mathcal{P}^{\text{ext}} = \int_C \mathbf{T}(\mathbf{x}, \mathbf{n}) \cdot \hat{\mathbf{v}}(\mathbf{x}) \, \mathrm{d}s + \int_A \mathbf{f}(\mathbf{x}) \cdot \hat{\mathbf{v}}(\mathbf{x}) \, \mathrm{d}A \tag{1}$$

with the volume forces $\mathbf{f}$, and traction forces $\mathbf{T}$, and $\mathbf{n}$ as the outward normal onto a surface element $\mathrm{d}C$. The power density of internal forces is constructed on the simplest velocity-derived quantity which is objective,

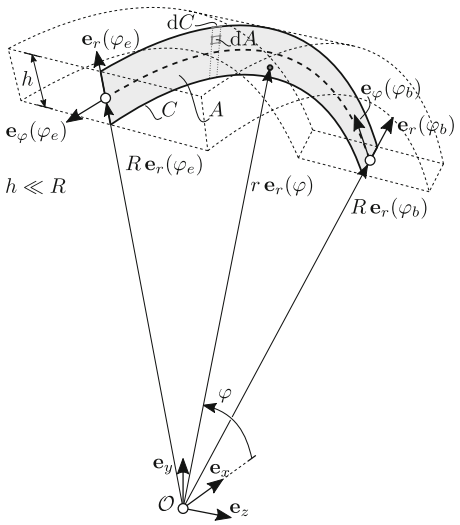

Fig. 1 Illustration of slender arch-like tunnel cross section with radius R and thickness h, global Cartesian base frame $\mathbf{e}_x$, $\mathbf{e}_y$, $\mathbf{e}_z$, and local polar base frame $\mathbf{e}_r(\varphi)$, $\mathbf{e}_\varphi(\varphi)$, $\mathbf{e}_z$; the latter is indicated at the beginning and the end of the segment, labeled by polar angles φ_b and φ_e

i.e., observer-independent. This is the Eulerian strain rate tensor

$$\hat{\mathbf{d}} = \nabla^S \hat{\mathbf{v}} = \frac{1}{2}\left[\frac{\partial \hat{\mathbf{v}}}{\partial \mathbf{x}} + \left(\frac{\partial \hat{\mathbf{v}}}{\partial \mathbf{x}}\right)^T\right]. \tag{2}$$

Accordingly, we have [9]

$$\mathcal{P}^{\text{int}} = -\int_A \boldsymbol{\sigma} : \hat{\mathbf{d}}\, \mathrm{d}A \tag{3}$$

whereby $\boldsymbol{\sigma}$ is the symmetric second-order Cauchy stress tensor - any non-symmetric tensor portion would not perform any power on $\hat{\mathbf{d}}$.

Mathematically, the principle of virtual power then reads as

$$\mathcal{P}^{\text{ext}}(\hat{\mathbf{v}}) + \mathcal{P}^{\text{int}}(\hat{\mathbf{d}}) = 0 \quad \forall \hat{\mathbf{v}}. \tag{4}$$

Application of the chain rule and of the divergence theorem to (4), together with (1) and (2), then readily yields [9]

$$\forall \mathbf{x} \in A : \text{div}\boldsymbol{\sigma} + \mathbf{f} = 0, \tag{5}$$

$$\forall \mathbf{x} \in C : \boldsymbol{\sigma} \cdot \mathbf{n} - \mathbf{T} = 0 \tag{6}$$

whereby all vectors occurring in (5) and (6) are restricted to the cross-sectional plane.

2.2 Virtual velocity field characterizing a slender circular tunnel shell segment

The principle of virtual power is particularly suitable tool for deriving theories for structural components, such as beams, arches, or plates [13,16,34,40]. In this context, the virtual velocity field governing the equilibrium conditions is further restricted; and this yields differential equations of lower dimensions than those of (5) and (6). In the case of circular cylindrical shell segments, the following characteristics are considered: The circular arch is geometrically defined by a segment of a circle with radius R (the arch line) and by the thickness h, see Fig. 1. The latter coincides with the length of straight generator lines lying perpendicular to the arch line. h needs to be scale separated from R, i.e., $h \ll R$. Positions which are relevant for the distribution of physical quantities throughout the circular segment defining the arch are given by location vectors $\mathbf{r}$,

$$\mathbf{r} = r\, \mathbf{e}_r(\varphi), \text{ for } r \in \left[R - h/2;\, R + h/2\right] \tag{7}$$

with r and φ standing for the radial and circumferential polar coordinate, respectively; $\mathbf{e}_r(\varphi)$, $\mathbf{e}_\varphi(\varphi)$, and $\mathbf{e}_z$ are the unit vectors spanning a corresponding orthonormal frame. More precisely, φ is the angle which is measured counterclockwisely from the base vector $\mathbf{e}_x$ of a Cartesian base frame made up by the base frame $\mathbf{e}_x$, $\mathbf{e}_y$, and $\mathbf{e}_z$ and the origin $\mathcal{O}$, see Fig. 1. The radius R and the polar angle φ give access to the arc length s,

$$s = R\varphi. \tag{8}$$

Each generator line of the circular slender arch is characterized by the following rigid body motions, see Fig. 2:

- it undergoes a translational motion orthogonal to the circle within the plane of the circle, quantified by a virtual velocity $\mathbf{e}_r \hat{v}_r^C$, with $\hat{v}_r^C$ being the radial component of the virtual velocity of the gravitational center of the generator line;
- it undergoes a rotational motion around the center of the circle (i.e., around a vector directed in $\mathbf{e}_z$ and positioned in the origin "$\mathcal{O}$" of the coordinate system seen in Fig. 1), quantified by a virtual velocity $\mathbf{e}_\varphi \hat{v}_\varphi^C\, r/R$, with $\hat{v}_\varphi^C$ being the circumferential component of the virtual velocity of the gravitational center of the generator line;
- it undergoes a rotational motion around a vector directed in $\mathbf{e}_z$ and positioned in the gravitational center of the generator line, quantified by a virtual velocity $\mathbf{e}_\varphi \hat{\omega}_z^C\, (r - R)$, with the virtual angular velocity component denoted as $\hat{\omega}_z^C$. The latter is chosen such that the cross-section remains orthogonal to the (virtually deformed) center surface of the shell segment, i.e.,

$$\frac{\mathrm{d}\hat{v}_r^C}{\mathrm{d}s} = \frac{\mathrm{d}\hat{v}_r^C}{\mathrm{d}\varphi}\frac{\mathrm{d}\varphi}{\mathrm{d}s} = \frac{1}{R}\frac{\mathrm{d}\hat{v}_r^C}{\mathrm{d}\varphi} = -\hat{\omega}_z^C \tag{9}$$

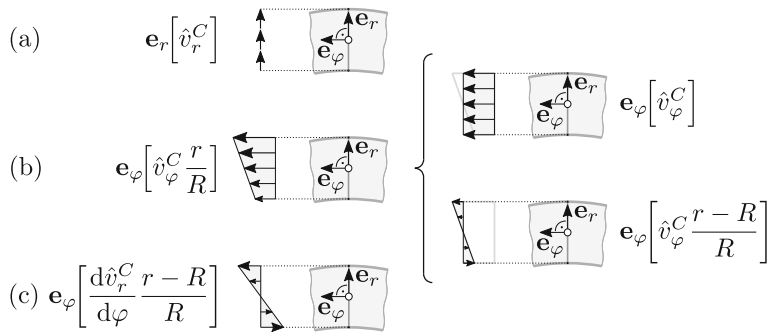

Fig. 2 Illustration of the virtual rigid body motions associated with an arbitrary generator of the circular segment: **a** translational motion orthogonal to the circle within the plane of the circle, **b** $\mathbf{e}_z$-associated rotational motion around the center of the circle as a superposition of a tangential translation of the gravitational center of the generator and a rotation around the latter center, **c** $\mathbf{e}_z$-associated rotational motion around the gravitational center of the generator of the circular arch

where we also made use of (8). Conclusively, the virtual velocity field governing the equilibrium of the circular arch segment reads as

$$\hat{\mathbf{v}} = \mathbf{e}_r \hat{v}_r^C + \mathbf{e}_\varphi \left[\hat{v}_\varphi^C \frac{r}{R} - \frac{1}{R} \frac{\mathrm{d}\hat{v}_r^C}{\mathrm{d}\varphi} (r - R) \right]. \tag{10}$$

However, for the development of structural theories of stretching and bending members, it is advisable to introduce $\mathbf{e}_z$-related rotations around the gravitational center of the generator (associated with bending) and translations in tangential direction (associated with stretching). Accordingly, we consider the rotation around the center of the circle as a superposition of a tangential translation of the gravitational center of the generator and a rotation around the latter center; mathematically, this reads as

$$\hat{v}_\varphi^C \frac{r}{R} = \hat{v}_\varphi^C + \hat{v}_\varphi^C \frac{r - R}{R}; \tag{11}$$

see the sketches at the right handside of Fig. 2.

2.3 Virtual power of internal forces—axial forces and bending moments in the tunnel shell

The components of the Eulerian strain rate tensor in a polar base frame read as, see e.g., [26, p. 747]

$$\hat{d}_{rr} = \frac{\partial \hat{v}_r}{\partial r}, \quad \hat{d}_{r\varphi} = \frac{1}{2} \left(\frac{1}{r} \frac{\partial \hat{v}_r}{\partial \varphi} + \frac{\partial \hat{v}_\varphi}{\partial r} - \frac{\hat{v}_\varphi}{r} \right) \tag{12.1}$$

$$\hat{d}_{\varphi\varphi} = \frac{1}{r} \frac{\partial \hat{v}_\varphi}{\partial \varphi} + \frac{\hat{v}_r}{r}, \quad \hat{d}_{rz} = \frac{1}{2} \left(\frac{\partial \hat{v}_z}{\partial r} + \frac{\partial \hat{v}_r}{\partial z} \right) \tag{12.2}$$

$$\hat{d}_{zz} = \frac{\partial \hat{v}_z}{\partial z}, \quad \hat{d}_{\varphi z} = \frac{1}{2} \left(\frac{\partial \hat{v}_\varphi}{\partial z} + \frac{1}{r} \frac{\partial \hat{v}_z}{\partial \varphi} \right) \tag{12.3}$$

and insertion of (10) and (11) into (12.2) yields

$$\hat{d}_{\varphi\varphi} = \frac{1}{r} \left[\hat{v}_r^C + \frac{\mathrm{d}\hat{v}_\varphi^C}{\mathrm{d}\varphi} \right] - \frac{r - R}{rR} \left[\frac{\mathrm{d}^2 \hat{v}_r^C}{\mathrm{d}\varphi^2} - \frac{\mathrm{d}\hat{v}_\varphi^C}{\mathrm{d}\varphi} \right] \tag{13}$$

while

$$\hat{d}_{rr} = \hat{d}_{r\varphi} = \hat{d}_{rz} = \hat{d}_{\varphi z} = \hat{d}_{zz} = 0. \tag{14}$$

Specification of the internal power expression (3) for the shell-specific virtual strain rates (13) and (14) yields

$$\mathcal{P}^{\mathrm{int}} = - \int_{\varphi_b}^{\varphi_e} \int_{R-h/2}^{R+h/2} \sigma_{\varphi\varphi}(r, \varphi) \left\{ \frac{\hat{v}_r^C(\varphi)}{r} + \frac{1}{r} \frac{\mathrm{d}\hat{v}_\varphi^C(\varphi)}{\mathrm{d}\varphi} - \frac{r - R}{rR} \left[\frac{\mathrm{d}^2 \hat{v}_r^C(\varphi)}{\mathrm{d}\varphi^2} - \frac{\mathrm{d}\hat{v}_\varphi^C(\varphi)}{\mathrm{d}\varphi} \right] \right\} r \, \mathrm{d}r \, \mathrm{d}\varphi \tag{15}$$

whereby φ_b and φ_e are the values of the polar angle at the beginning and at the end of the tunnel segment, respectively. Taking all terms independent of r out of the respective integral, expression (15) for the virtual power of the internal forces can be transformed to

$$\begin{aligned}\mathcal{P}^{\text{int}} &= -\int_{\varphi_b}^{\varphi_e}\left[\hat{v}_r^C + \frac{\mathrm{d}\hat{v}_\varphi^C}{\mathrm{d}\varphi}\right]\int_{R-h/2}^{R+h/2}\sigma_{\varphi\varphi}\,\mathrm{d}r\,\mathrm{d}\varphi + \frac{1}{R}\int_{\varphi_b}^{\varphi_e}\left[\frac{\mathrm{d}^2\hat{v}_r^C}{\mathrm{d}\varphi^2} - \frac{\mathrm{d}\hat{v}_\varphi^C}{\mathrm{d}\varphi}\right]\int_{R-h/2}^{R+h/2}\sigma_{\varphi\varphi}(r-R)\,\mathrm{d}r\,\mathrm{d}\varphi \\ &= -\int_{\varphi_b}^{\varphi_e}\left[\hat{v}_r^C + \frac{\mathrm{d}\hat{v}_\varphi^C}{\mathrm{d}\varphi}\right]n_\varphi\,\mathrm{d}\varphi + \frac{1}{R}\int_{\varphi_b}^{\varphi_e}\left[\frac{\mathrm{d}^2\hat{v}_r^C}{\mathrm{d}\varphi^2} - \frac{\mathrm{d}\hat{v}_\varphi^C}{\mathrm{d}\varphi}\right]m_\varphi\,\mathrm{d}\varphi\end{aligned} \tag{16}$$

whereby the separate integration over r has induced the new, shell-specific internal forces called axial forces (per length)

$$n_\varphi(\varphi) = \int_{R-h/2}^{R+h/2}\sigma_{\varphi\varphi}(r,\varphi)\,\mathrm{d}r \tag{17}$$

and bending moments (per length)

$$m_\varphi(\varphi) = \int_{R-h/2}^{R+h/2}\sigma_{\varphi\varphi}(r,\varphi)\times(r-R)\,\mathrm{d}r. \tag{18}$$

It becomes obvious from (13) and (16)–(18) that axial forces perform power on strain rates stemming from virtual translational motions of the cross sections in the tangential direction, while the bending moments perform power on strain rates stemming from virtual rotational motions around the gravitational centers of the generator lines.

2.4 Virtual power of external forces—ground pressure and impost forces

In tunnel shells, the external forces due to dead load (gravitational forces) are typically negligible with respect to the tractions forces stemming from the action of the surrounding ground, at radial coordinate $r = R + h/2$, so that $|\mathbf{T}| \gg h\,|\mathbf{f}|$ in expression (1) for the virtual power of the external forces. Furthermore, relevant traction forces occur only at surfaces with normals $+\mathbf{e}_r(\varphi)$, $-\mathbf{e}_\varphi(\varphi_b)$, and $+\mathbf{e}_\varphi(\varphi_e)$. Considering these specifications, the insertion of the shell-specific virtual velocities (10) into expression (1) for the external forces acting in an arch-like tunnel cross section yields

$$\begin{aligned}\mathcal{P}^{\text{ext}} = &+\int_{\varphi_b}^{\varphi_e} T_r\big[r = R + h/2, \varphi; \mathbf{n} = +\mathbf{e}_r(\varphi)\big]\left\{\hat{v}_r^C(\varphi)\right\}(R + h/2)\,\mathrm{d}\varphi \\ &+\int_{R-h/2}^{R+h/2} T_\varphi\big[r, \varphi; \mathbf{n} = \pm\mathbf{e}_\varphi(\varphi)\big]\,\mathrm{d}r\left\{\hat{v}_\varphi^C(\varphi)\right\}\Big|_{\varphi_b}^{\varphi_e}.\end{aligned} \tag{19}$$

Considering $h \ll R$, (19) can be simplified to

$$\mathcal{P}^{\text{ext}} = +\int_{\varphi_b}^{\varphi_e} -G_p(\varphi)\left\{\hat{v}_r^C(\varphi)R\right\}\,\mathrm{d}\varphi - N_p(\varphi)\left\{\hat{v}_\varphi^C(\varphi)\right\}\Big|_{\varphi_b}^{\varphi_e} \tag{20}$$

whereby we introduced the tunnel engineering-specific notions of ground pressure, reading as

$$G_p(\varphi) = -T_r\big[r = R + h/2, \varphi; \mathbf{n} = \mathbf{e}_r(\varphi)\big] \tag{21}$$

and axial forces $N_{p,b} = N_p(\varphi_b)$ and $N_{p,e} = N_p(\varphi_e)$ at the beginning and at the end of the tunnel segment. Resorting to architectural terms, the latter may be called impost forces. Defining them, somewhat analogously to the ground pressure (21), as compressive forces, they read mathematically as

$$N_{p,b} = \int_{R-h/2}^{R+h/2} T_\varphi\big[r, \varphi_b; \mathbf{n} = -\mathbf{e}_\varphi(\varphi_b)\big]\,\mathrm{d}r = -\int_{R-h/2}^{R+h/2} \sigma_{\varphi\varphi}(r, \varphi_b)\,\mathrm{d}r = -n_\varphi(\varphi_b) \tag{22}$$

and

$$N_{p,e} = -\int_{R-h/2}^{R+h/2} T_\varphi\big[r, \varphi_e; \mathbf{n} = +\mathbf{e}_\varphi(\varphi_e)\big]\,\mathrm{d}r = -\int_{R-h/2}^{R+h/2} \sigma_{\varphi\varphi}(r, \varphi_e)\,\mathrm{d}r = -n_\varphi(\varphi_e) \tag{23}$$

whereby use of (17) and (6) with $\mathbf{n} = -\mathbf{e}_x$ and $\mathbf{n} = \mathbf{e}_x$, respectively, was made.

2.5 Principle of virtual power—differential equilibrium conditions

In order to obtain differential equations quantifying the equilibrium in the tunnel shell segment, expression (4) for the principle of virtual power is considered to hold for the virtual velocity format (10) with arbitrary shell-specific virtual velocity fields $\hat{v}_r^C$ and $\hat{v}_\varphi^C$. Therefore, Eq. (4) needs to be combined with the shell-specific expressions (16) and (20) for the power of the internal and the external forces, respectively; and the latter need to undergo partial integration. For the internal forces, we get

$$\begin{aligned}\mathcal{P}^{\mathrm{int}} = &+\int_{\varphi_b}^{\varphi_e}\left[-n_\varphi + \frac{1}{R}\frac{\mathrm{d}^2 m_\varphi}{\mathrm{d}\varphi^2}\right]\hat{v}_r^C\,\mathrm{d}\varphi - \left[\frac{1}{R}\frac{\mathrm{d}m_\varphi}{\mathrm{d}\varphi}\right]\hat{v}_r^C\Big|_{\varphi_b}^{\varphi_e} \\ &+\int_{\varphi_b}^{\varphi_e}\left[\frac{\mathrm{d}n_\varphi}{\mathrm{d}\varphi} + \frac{1}{R}\frac{\mathrm{d}m_\varphi}{\mathrm{d}\varphi}\right]\hat{v}_\varphi^C\,\mathrm{d}\varphi - \big[n_\varphi\big]\hat{v}_\varphi^C\Big|_{\varphi_b}^{\varphi_e}\end{aligned} \tag{24}$$

whereby we considered vanishing bending moments at the surfaces with $\varphi = \varphi_b$ and $\varphi = \varphi_e$,

$$m_\varphi(\varphi_b) = 0; \quad m_\varphi(\varphi_e) = 0, \tag{25.1,2}$$

Insertion of (24) and (20) into Eq. (4), and requiring the result to hold for arbitrary values of $\hat{v}_r^C$ and $\hat{v}_\varphi^C$ yields the differential equilibrium conditions valid along the entire arch segment,

$$\text{for } \varphi_b \le \varphi \le \varphi_e: \quad -n_\varphi + \frac{1}{R}\frac{\mathrm{d}^2 m_\varphi}{\mathrm{d}\varphi^2} - RG_p = 0, \tag{26.1}$$

$$\frac{\mathrm{d}n_\varphi}{\mathrm{d}\varphi} + \frac{1}{R}\frac{\mathrm{d}m_\varphi}{\mathrm{d}\varphi} = 0 \tag{26.2}$$

as well as the natural boundary conditions valid at the beginning and the end of the tunnel segment,

$$\text{for } \varphi = \varphi_b \text{ and } \varphi = \varphi_e: \quad -\frac{1}{R}\frac{\mathrm{d}m_\varphi}{\mathrm{d}\varphi} = 0. \tag{27}$$

2.6 Ground pressure-induced distributions of internal axial forces and bending moments in tunnel shell segment

As a first step to obtain mathematical solutions for the differential equations (26.1), (26.2) is differentiated with respect to φ, and the corresponding result is solved for $(1/R)(\mathrm{d}^2 m_\varphi/\mathrm{d}\varphi^2)$, yielding

$$\frac{1}{R}\frac{\mathrm{d}^2 m_\varphi}{\mathrm{d}\varphi^2} = -\frac{\mathrm{d}^2 n_\varphi}{\mathrm{d}\varphi^2}, \tag{28}$$

This equation is then re-inserted into (26.1), yielding a differential equation for $n(\varphi)$ only. The latter reads as

$$n_\varphi + \frac{\mathrm{d}^2 n_\varphi}{\mathrm{d}\varphi^2} + RG_p = 0. \tag{29}$$

This differential equation can be readily integrated for given functions quantifying the ground pressure distribution along the circumferential coordinate φ. In the following, we are interested in simple functional forms which eventually allow for conversion of displacement components from three geodetic measurement points into ground pressure values defined at four points along the circumferential coordinate φ. In more detail, we consider the weighted superposition of four cubic shape functions, the values of which are either one or zero at equi-distant points along the coordinate $\bar{\varphi} = \varphi - \varphi_b$. In the case of cubic polynomials, we have for the ground pressure

$$G_p = A_1(\bar{\varphi})G_{p,1} + A_2(\bar{\varphi})G_{p,2} + A_3(\bar{\varphi})G_{p,3} + A_4(\bar{\varphi})G_{p,4}. \tag{30}$$

Thereby, the cubic polynomials A_i, $i = 1, 2, 3, 4$, read as

$$\begin{aligned}
A_1(\bar{\varphi}) &= 1 - \frac{11\bar{\varphi}}{2\Delta\varphi} + \frac{9\bar{\varphi}^2}{(\Delta\varphi)^2} - \frac{9\bar{\varphi}^3}{2(\Delta\varphi)^3},\\
A_2(\bar{\varphi}) &= \frac{9\bar{\varphi}}{\Delta\varphi} - \frac{45\bar{\varphi}^2}{2(\Delta\varphi)^2} + \frac{27\bar{\varphi}^3}{2(\Delta\varphi)^3},\\
A_3(\bar{\varphi}) &= -\frac{9\bar{\varphi}}{2\Delta\varphi} + \frac{18\bar{\varphi}^2}{(\Delta\varphi)^2} - \frac{27\bar{\varphi}^3}{2(\Delta\varphi)^3},\\
A_4(\bar{\varphi}) &= \frac{\bar{\varphi}}{\Delta\varphi} - \frac{9\bar{\varphi}^2}{2(\Delta\varphi)^2} + \frac{9\bar{\varphi}^3}{2(\Delta\varphi)^3}
\end{aligned} \tag{31}$$

with $\Delta\varphi = \varphi_e - \varphi_b$ the opening angle of the tunnel shell. In (30), $G_{p,1}$ is the pressure at position $\bar{\varphi} = 0$, $G_{p,2}$ is the pressure at position $\bar{\varphi} = \Delta\varphi/3$, $G_{p,3}$ is the pressure at position $\bar{\varphi} = 2\Delta\varphi/3$, and $G_{p,4}$ is the pressure at position $\bar{\varphi} = \Delta\varphi$.

The solution of the differential equation (29) for the ground pressure according to (30) and (31) yields

$$\begin{aligned}
n_\varphi(\bar{\varphi}) = {} & +N_{p,b}\left\{\cos(\bar{\varphi}) - \frac{\sin(\bar{\varphi})}{\tan(\Delta\varphi)}\right\} + N_{p,e}\left\{\frac{\sin(\bar{\varphi})}{\sin(\Delta\varphi)}\right\}\\
& - RG_{p,1}\left\{1 + \frac{27\bar{\varphi}}{(\Delta\varphi)^3} - \frac{9\bar{\varphi}^3}{2(\Delta\varphi)^3} - \frac{18}{(\Delta\varphi)^2} + \frac{9\bar{\varphi}^2}{(\Delta\varphi)^2} - \frac{11\bar{\varphi}}{2\Delta\varphi} - \cos(\bar{\varphi})\right.\\
& \left. + \frac{18\cos(\bar{\varphi})}{(\Delta\varphi)^2} + \frac{\sin(\bar{\varphi})}{\tan(\Delta\varphi)} - \frac{18\sin(\bar{\varphi})}{(\Delta\varphi)^2\tan(\Delta\varphi)} - \frac{9\sin(\bar{\varphi})}{(\Delta\varphi)^2\sin(\Delta\varphi)}\right\}\\
& - RG_{p,2}\left\{-\frac{81\bar{\varphi}}{(\Delta\varphi)^3} + \frac{27\bar{\varphi}^3}{2(\Delta\varphi)^3} + \frac{45}{(\Delta\varphi)^2} - \frac{45\bar{\varphi}^2}{2(\Delta\varphi)^2} + \frac{9\bar{\varphi}}{\Delta\varphi}\right.\\
& \left. - \frac{45\cos(\bar{\varphi})}{(\Delta\varphi)^2} + \frac{45\sin(\bar{\varphi})}{(\Delta\varphi)^2\tan(\Delta\varphi)} + \frac{36\sin(\bar{\varphi})}{(\Delta\varphi)^2\sin(\Delta\varphi)}\right\}\\
& - RG_{p,3}\left\{\frac{81\bar{\varphi}}{(\Delta\varphi)^3} - \frac{27\bar{\varphi}^3}{2(\Delta\varphi)^3} - \frac{36}{(\Delta\varphi)^2} + \frac{18\bar{\varphi}^2}{(\Delta\varphi)^2} - \frac{9\bar{\varphi}}{2\Delta\varphi}\right.\\
& \left. + \frac{36\cos(\bar{\varphi})}{(\Delta\varphi)^2} - \frac{36\sin(\bar{\varphi})}{(\Delta\varphi)^2\tan(\Delta\varphi)} - \frac{45\sin(\bar{\varphi})}{(\Delta\varphi)^2\sin(\Delta\varphi)}\right\}
\end{aligned}$$

$$
\begin{aligned}
&-RG_{p,4}\left\{-\frac{27\bar{\varphi}}{(\Delta\varphi)^3}+\frac{9\bar{\varphi}^3}{2(\Delta\varphi)^3}+\frac{9}{(\Delta\varphi)^2}-\frac{9\bar{\varphi}^2}{2(\Delta\varphi)^2}+\frac{\bar{\varphi}}{\Delta\varphi}\right.\\
&\left.-\frac{9\cos(\bar{\varphi})}{(\Delta\varphi)^2}+\frac{9\sin(\bar{\varphi})}{(\Delta\varphi)^2\tan(\Delta\varphi)}-\frac{\sin(\bar{\varphi})}{\sin(\Delta\varphi)}+\frac{18\sin(\bar{\varphi})}{(\Delta\varphi^2)\sin(\Delta\varphi)}\right\}
\end{aligned}
\tag{32}
$$

where we considered Eqs. (22) and (23) to label the forces $N_{p,b}$ and $N_{p,e}$ pressing from the outside onto the imposts of the considered tunnel shell segment. The solution of the differential equation (26.1) for the ground pressure according to Eqs. (30) and (31), and for the axial forces according Eq. (32) yields

$$
\begin{aligned}
m_\varphi(\bar{\varphi}) = &+RN_{p,b}\left\{1-\cos(\bar{\varphi})+\frac{\sin(\bar{\varphi})}{\tan(\Delta\varphi)}\right\}-RN_{p,e}\left\{\frac{\sin(\bar{\varphi})}{\sin(\Delta\varphi)}\right\}\\
&-R^2G_{p,1}\left\{-1-\frac{27\bar{\varphi}}{(\Delta\varphi)^3}+\frac{9\bar{\varphi}^3}{2(\Delta\varphi)^3}+\frac{18}{(\Delta\varphi)^2}-\frac{9\bar{\varphi}^2}{(\Delta\varphi)^2}+\frac{11\bar{\varphi}}{2\Delta\varphi}+\cos(\bar{\varphi})\right.\\
&\left.-\frac{18\cos(\bar{\varphi})}{(\Delta\varphi)^2}-\frac{\sin(\bar{\varphi})}{\tan(\Delta\varphi)}+\frac{18\sin(\bar{\varphi})}{(\Delta\varphi)^2\tan(\Delta\varphi)}+\frac{9\sin(\bar{\varphi})}{(\Delta\varphi)^2\sin(\Delta\varphi)}\right\}\\
&-R^2G_{p,2}\left\{\frac{81\bar{\varphi}}{(\Delta\varphi)^3}-\frac{27\bar{\varphi}^3}{2(\Delta\varphi)^3}-\frac{45}{(\Delta\varphi)^2}+\frac{45\bar{\varphi}^2}{2(\Delta\varphi)^2}-\frac{9\bar{\varphi}}{\Delta\varphi}\right.\\
&\left.+\frac{45\cos(\bar{\varphi})}{(\Delta\varphi)^2}-\frac{45\sin(\bar{\varphi})}{(\Delta\varphi)^2\tan(\Delta\varphi)}-\frac{36\sin(\bar{\varphi})}{(\Delta\varphi)^2\sin(\Delta\varphi)}\right\}\\
&-R^2G_{p,3}\left\{-\frac{81\bar{\varphi}}{(\Delta\varphi)^3}+\frac{27\bar{\varphi}^3}{2(\Delta\varphi)^3}+\frac{36}{(\Delta\varphi)^2}-\frac{18\bar{\varphi}^2}{(\Delta\varphi)^2}+\frac{9\bar{\varphi}}{2\Delta\varphi}\right.\\
&\left.-\frac{36\cos(\bar{\varphi})}{(\Delta\varphi)^2}+\frac{36\sin(\bar{\varphi})}{(\Delta\varphi)^2\tan(\Delta\varphi)}+\frac{45\sin(\bar{\varphi})}{(\Delta\varphi)^2\sin(\Delta\varphi)}\right\}\\
&-R^2G_{p,4}\left\{\frac{27\bar{\varphi}}{(\Delta\varphi)^3}-\frac{9\bar{\varphi}^3}{2(\Delta\varphi)^3}-\frac{9}{(\Delta\varphi)^2}+\frac{9\bar{\varphi}^2}{2(\Delta\varphi)^2}-\frac{\bar{\varphi}}{\Delta\varphi}\right.\\
&\left.+\frac{9\cos(\bar{\varphi})}{(\Delta\varphi)^2}-\frac{9\sin(\bar{\varphi})}{(\Delta\varphi)^2\tan(\Delta\varphi)}+\frac{\sin(\bar{\varphi})}{\sin(\Delta\varphi)}-\frac{18\sin(\bar{\varphi})}{(\Delta\varphi)^2\sin(\Delta\varphi)}\right\}
\end{aligned}
\tag{33}
$$

whereby we considered vanishing bending moment at the beginning of the tunnel shell segment, see (25.1). Specification of (33) for $m_\varphi(\varphi_e) = m_\varphi(\bar{\varphi} = \Delta\varphi) = 0$ yields the remarkable result

$$
N_{p,b}R - N_{p,e}R = 0 \;\rightarrow\; N_{p,b} = N_{p,e}. \tag{34}
$$

In other words, independent of the actual ground pressure distribution, the impost forces at the beginning and the end of the tunnel segment are equal.

3 Strength, elasticity, and creep of shotcrete tunnel shells

3.1 Strength, elasticity, and creep properties of concrete—Laplace Carson transform into inverse time domain

For the purposes of practical concrete engineering, it is customary to approximate the temporal evolution of the uniaxial strength of concrete under isothermal conditions at 20 centigrades by a suitable fitting function, such as the one given in [4],

$$
f_c(t) = f_{c,28\mathrm{d}}\exp\left[s_E\left(1-\sqrt{\frac{28\ \mathrm{days}}{t}}\right)\right], \tag{35}
$$

with the dimensionless strength evolution parameter s_E, and with the time t being given in the unit of measurement "days" and being resolved down to tens of minutes. Typical values relevant for shotcrete tunneling are given in Table 1 and illustrated in Fig. 3a. Analogous relationships are employed for the elasticity development,

$$
E(t) = E_{28\mathrm{d}}\left\{\exp\left[s_E\left(1-\sqrt{\frac{28\ \mathrm{days}}{t}}\right)\right]\right\}^{0.5}, \tag{36}
$$

Table 1 Optimal dimensionless parameters s_E, s_{E_c} for three typical cement types [1]

Cement type	s_E	s_{E_c}
CEM II/A-M(S-L) 42.5N	0.22	0.62
CEM II/A-S 42.5R	0.18	0.61
CEM I 52.5R	0.09	0.50

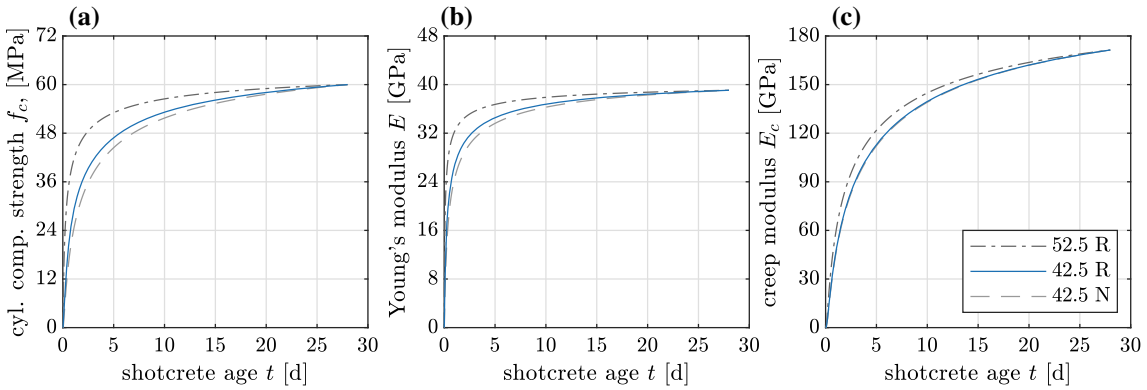

Fig. 3 Temporal evolution of material properties of shotcrete with the uniaxial 28-day compressive strength $f_{c,28\mathrm{d}} = 60$ MPa [38], and the different cement types given in Table 1: **a** uniaxial compressive strength, **b** Young's modulus, **c** creep modulus

with

$$E_{28\mathrm{d}} = 21.5\,\mathrm{GPa} \times \alpha \left(\frac{f_{c,28\mathrm{d}}}{10\,\mathrm{MPa}} \right)^{0.\dot{3}}; \tag{37}$$

see again Table 1 and Fig. 3b for typical values concerning shotcrete, and the parameter α amounts to one for quartz- and limestone-based concretes [1].

Both the uniaxial strength and Young's modulus are driven by the hydration reaction leading to changes in the material's microstructure, and this can be quantified by multiscale micromechanical models such as the one proposed in [18] and employed in [39]. In more detail, the uniaxial strength is governed by the hydration degree, the (initial) water-to-cement ratio, and the aggregate volume fraction in an RVE of concrete (see Appendix A), which allows one to reconstruct the evolution of the hydration degree associated with property developments (35) and (36) as

$$\xi(t) = \xi \left[f_c(t),\, w/c,\, f_{\mathrm{agg}}^{\mathrm{con}} \right], \tag{38}$$

see Fig. 4. The degree of hydration also governs the (ultra-)short term creep of concrete, as evidenced by three-minute creep tests [1,14,33], which give access to power-law type creep functions describing creep over time spans during which the hydration degree is virtually constant (i.e., from minutes in early-age concrete, to weeks in decade-old concrete [17]),

$$J(\xi, t) = \frac{1}{E(\xi)} + \frac{1}{E_c(\xi)} \left[\frac{t}{t_0} \right]^{\beta}, \tag{39}$$

with t being resolved down to the time regime of seconds, with the power-law exponent amounting typically to 0.25 [17], with the creep modulus E_c and Young's modulus E depending on the degree of hydration ξ, and with $t_0 = 1\,\mathrm{d} = 86\,400\,\mathrm{s}$ as a reference time. E_c is also available from isothermal creep tests performed at a temperature of 20 centigrades [1], namely in the format

$$E_c(t) = E_{c,28\mathrm{d}} \left\{ \exp \left[s_{E_c} \left(1 - \sqrt{\frac{28\,\mathrm{days}}{t}} \right) \right] \right\}^{0.5} \tag{40}$$

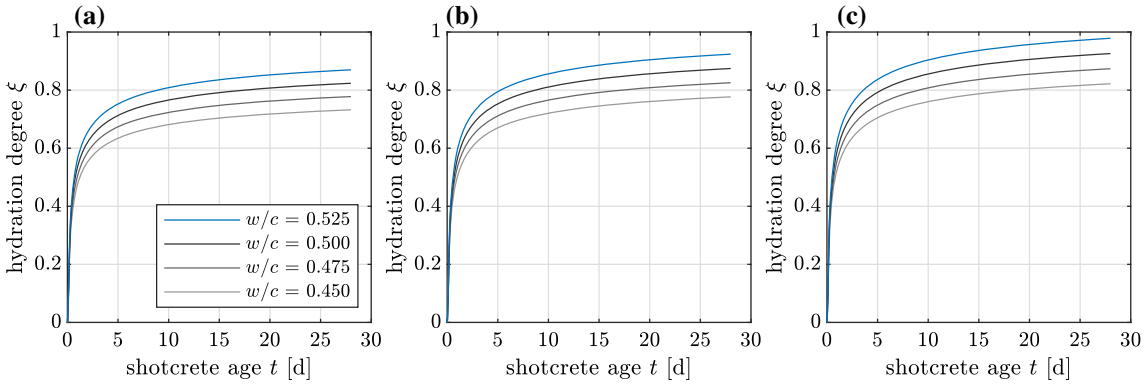

Fig. 4 Temporal evolution of the hydration degree according to (38), in combination with (35) and (90)–(98), with the aggregate volume fraction amounting to $f_{\text{agg}}^{\text{con}} = 0.70$, the effective water-to-cement mass ratios taken from the set $(w/c)_{eff} \in \{0.450, 0.475, 0.500, 0.525\}$, the strength evolution parameter $s_E = 0.18$, and three different strength values reached at an age of 28 days: **a** $f_{c,28\text{d}} = 50\,\text{MPa}$, **b** $f_{c,28\text{d}} = 55\,\text{MPa}$, **c** $f_{c,28\text{d}} = 60\,\text{MPa}$

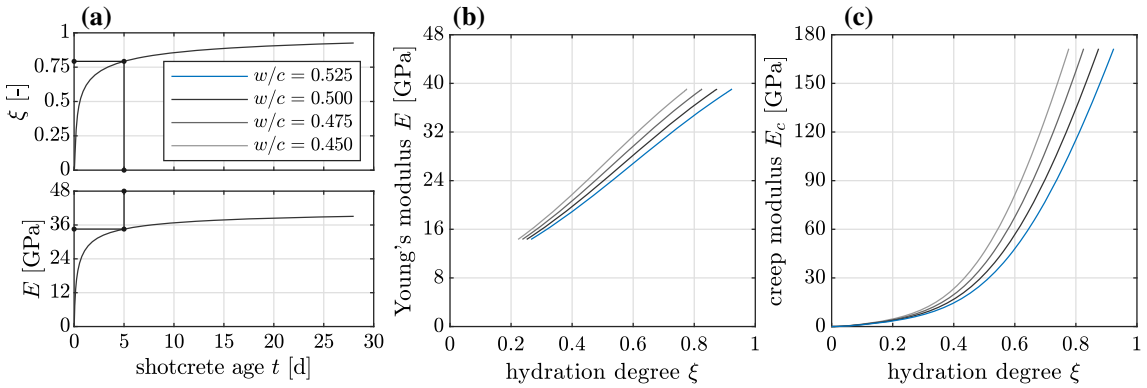

Fig. 5 Reconstruction of maturity-property relations $E(\xi)$ and $E_c(\xi)$ for uniaxial 28-day compressive strength $f_{c,28\text{d}} = 60\,\text{MPa}$ and cement type 42.5R (see Table 1): **a** data pair identification from temporal evolutions of Young's modulus and degree of hydration; **b** Young's modulus as function of degree of hydration; **c** creep modulus as function of degree of hydration

with

$$E_{c,28\text{d}} = 51.9\,\text{GPa}\left(\alpha\,\frac{f_{c,28\text{d}}}{10\,\text{MPa}}\right)^{2/3}, \tag{41}$$

Accordingly, evaluation of (36) and (40) at the same time instants, and forming corresponding data pairs of hydration degree and (Young's or creep) modulus, gives access to the material functions $E(\xi)$, $E_c(\xi)$, see Fig. 5.

$J(\xi, t)$ describes the behavior of a material sample with (constant) degree of hydration ξ, under uniaxial stress $\boldsymbol{\sigma} = \sigma_{\varphi\varphi}\,\mathbf{e}_\varphi \otimes \mathbf{e}_\varphi$, according to a hereditary integral of the Boltzmann type [3,20],

$$\varepsilon_{\varphi\varphi}(\xi, t) = \int_{-\infty}^{t} J(\xi, t-\tau)\,\dot{\sigma}_{\varphi\varphi}(\tau)\,\mathrm{d}\tau, \tag{42}$$

which, after Laplace-Carson transformation

$$f(p) = p\int_{0}^{\infty} f(t)\exp(-pt)\,\mathrm{d}t \tag{43}$$

reads as

$$\varepsilon_{\varphi\varphi}(\xi, p) = J(\xi, p)\,\sigma_{\varphi\varphi}(p) \tag{44}$$

with the transformed function $J(\xi, p)$ exhibiting the format

$$J(\xi, p) = \frac{1}{E(\xi)} + \frac{\Gamma(1+\beta)}{E_c(\xi)\, p^{\beta}} \left[\frac{1}{t_0}\right]^{\beta}. \tag{45}$$

Lateral normal strains are customarily considered by a constant Poisson's ratio of $\nu = 0.2$, in the form

$$\varepsilon_{rr}(\xi, p) = \varepsilon_{zz}(\xi, p) = -\nu\, \varepsilon_{\varphi\varphi}(\xi, p), \tag{46}$$

and in a fully 3D isotropic setting, (44) reads as

$$\begin{bmatrix} \varepsilon_{\varphi\varphi}(\xi, p) \\ \varepsilon_{rr}(\xi, p) \\ \varepsilon_{zz}(\xi, p) \end{bmatrix} = \begin{bmatrix} J(\xi, p) & -\nu J(\xi, p) & -\nu J(\xi, p) \\ -\nu J(\xi, p) & J(\xi, p) & -\nu J(\xi, p) \\ -\nu J(\xi, p) & -\nu J(\xi, p) & J(\xi, p) \end{bmatrix} \cdot \begin{bmatrix} \sigma_{\varphi\varphi}(p) \\ \sigma_{rr}(p) \\ \sigma_{zz}(p) \end{bmatrix}. \tag{47}$$

However, tunnel shells, as a rule, do not undergo uniaxial stresses; in fact, as a first approximation, they are rather characterized by $\varepsilon_{zz}(p) \approx 0$. Corresponding specification of (47) and solution for the unknowns $\sigma_{\varphi\varphi}(p)$ and $\sigma_{zz}(p)$ yields

$$\sigma_{\varphi\varphi}(\xi, p) = R_{\text{ax}}^{\text{shell}}(\xi, p)\, \varepsilon_{\varphi\varphi}(p), \tag{48.1}$$

$$\sigma_{zz}(\xi, p) = R_{\text{lat}}^{\text{shell}}(\xi, p)\, \varepsilon_{\varphi\varphi}(p) \tag{48.2}$$

with

$$R_{\text{ax}}^{\text{shell}}(\xi, p) = \frac{1}{(1-\nu^2) J(\xi, p)}, \tag{49.1}$$

$$R_{\text{lat}}^{\text{shell}}(\xi, p) = \frac{\nu}{(1+\nu) J(\xi, p)}. \tag{49.2}$$

We note that Eqs. (48) and (49) describe the stress reaction of a piece of shotcrete with hydration degree ξ, situated within the tunnel shell, to normal strain $\varepsilon_{\varphi\varphi}$ evolving with the inverse time variable p.

3.2 Creep upscaling from material to shell level—backtransformation into the time domain

In order to relate the stress resultants n_φ and m_φ, see Eqs. (17) and (18), to the strains they provoke, (48.1) is inserted into (17) and (18), respectively, yielding

$$n_\varphi(\xi, \varphi, p) = \int_{R-h/2}^{R+h/2} R_{\text{ax}}^{\text{shell}}(\xi, p) \times \varepsilon_{\varphi\varphi}(r, \varphi, p)\, \mathrm{d}r \tag{50.1}$$

$$m_\varphi(\xi, \varphi, p) = \int_{R-h/2}^{R+h/2} (r - R) \times R_{\text{ax}}^{\text{shell}}(\xi, p) \times \varepsilon_{\varphi\varphi}(r, \varphi, p)\, \mathrm{d}r \tag{50.2}$$

where we consider, for the sake of simplicity, homogeneous viscoelastic properties within the tunnel shell segment; these properties being still associated with a constant degree of hydration ξ. The tangential normal strains $\varepsilon_{\varphi\varphi}$ and the corresponding tangential and radial displacements are introduced in a linearized fashion, by temporal integration over constant strain rates which are formally identical with (13); this results straightforwardly in

$$\begin{aligned} \varepsilon_{\varphi\varphi} &= \frac{1}{r} u_r^C + \frac{1}{R} \frac{\mathrm{d}u_\varphi^C}{\mathrm{d}\varphi} - \frac{r-R}{rR} \frac{\mathrm{d}^2 u_r^C}{\mathrm{d}\varphi^2} \\ &= \frac{1}{r} \left[u_r^C + \frac{\mathrm{d}u_\varphi^C}{\mathrm{d}\varphi} \right] - \frac{r-R}{rR} \left[\frac{\mathrm{d}^2 u_r^C}{\mathrm{d}\varphi^2} - \frac{\mathrm{d}u_\varphi^C}{\mathrm{d}\varphi} \right] \end{aligned} \tag{51}$$

whereby the term proportional to $(1/r)$ is related to stretching, while the bending-related term is proportional to $(r - R)$. Insertion of (51) into (50.1) yields

$$\begin{aligned} n_\varphi(\xi, \varphi, p) = R_{\mathrm{ax}}^{\mathrm{shell}}(\xi, p) \Bigg\{ & u_r^C(\varphi, p) \int_{R-h/2}^{R+h/2} \frac{1}{r}\,\mathrm{d}r + \frac{\mathrm{d}u_\varphi^C(\varphi, p)}{\mathrm{d}\varphi} \int_{R-h/2}^{R+h/2} \frac{1}{R}\,\mathrm{d}r \\ & - \frac{\mathrm{d}^2 u_r^C(\varphi, p)}{\mathrm{d}\varphi^2} \int_{R-h/2}^{R+h/2} \frac{r-R}{rR}\,\mathrm{d}r \Bigg\} \\ \approx R_{\mathrm{ax}}^{\mathrm{shell}}(\xi, p) & \frac{h}{R} \left[u_r^C(\varphi, p) + \frac{\mathrm{d}u_\varphi^C(\varphi, p)}{\mathrm{d}\varphi} \right] \end{aligned} \tag{52}$$

whereby the last term holds for $(h/R) \ll 1$, in particular because

$$\begin{aligned} \int_{R-h/2}^{R+h/2} \frac{1}{r}\,\mathrm{d}r &= \ln\left(R + \frac{h}{2}\right) - \ln\left(R - \frac{h}{2}\right) \\ &= \frac{h}{R} + \frac{1}{12}\left[\frac{h}{R}\right]^3 + \frac{1}{80}\left[\frac{h}{R}\right]^5 + \ldots \approx \frac{h}{R} \\ \int_{R-h/2}^{R+h/2} \frac{r-R}{rR}\,\mathrm{d}r &= \int_{R-h/2}^{R+h/2} \frac{1}{R}\,\mathrm{d}r - \int_{R-h/2}^{R+h/2} \frac{1}{r}\,\mathrm{d}r \\ &= \frac{h}{R} - \frac{h}{R} - \frac{1}{12}\left[\frac{h}{R}\right]^3 - \frac{R}{80}\left[\frac{h}{R}\right]^5 + \ldots \approx 0. \end{aligned} \tag{53}$$

Insertion of (51) into (50.2) yields

$$\begin{aligned} m_\varphi(\xi, \varphi, p) = R_{\mathrm{ax}}^{\mathrm{shell}}(\xi, p) \Bigg\{ & \left[u_r^C(\varphi, p) + \frac{\mathrm{d}u_\varphi^C(\varphi, p)}{\mathrm{d}\varphi} \right] \int_{R-h/2}^{R+h/2} \frac{r-R}{r}\,\mathrm{d}r \\ & - \left[\frac{\mathrm{d}^2 u_r^C(\varphi, p)}{\mathrm{d}\varphi^2} - \frac{\mathrm{d}u_\varphi^C(\varphi, p)}{\mathrm{d}\varphi} \right] \int_{R-h/2}^{R+h/2} \frac{(r-R)^2}{rR}\,\mathrm{d}r \Bigg\} \\ \approx R_{\mathrm{ax}}^{\mathrm{shell}}(\xi, p) & \frac{1}{12}\frac{h^3}{R^2} \left[\frac{\mathrm{d}u_\varphi^C(\varphi, p)}{\mathrm{d}\varphi} - \frac{\mathrm{d}^2 u_r^C(\varphi, p)}{\mathrm{d}\varphi^2} \right]. \end{aligned} \tag{54}$$

The last term in (54) holds for $(h/R) \ll 1$, because of the following considerations: Firstly, the integrals occurring in (54) can be evaluated as follows:

$$\begin{aligned} \int_{R-\frac{h}{2}}^{R+\frac{h}{2}} \frac{(r-R)^2}{rR}\,\mathrm{d}r &= -h + R\,\ln\left[\frac{R + h/2}{R - h/2}\right] \\ &= +R\left\{ \frac{1}{12}\left[\frac{h}{R}\right]^3 + \frac{1}{80}\left[\frac{h}{R}\right]^5 + \ldots \right\} \approx +\frac{1}{12}\frac{h^3}{R^2}, \\ \int_{R-h/2}^{R+h/2} \frac{r-R}{r}\,\mathrm{d}r &= \int_{R-h/2}^{R+h/2} 1\,\mathrm{d}r - \int_{R-h/2}^{R+h/2} \frac{R}{r}\,\mathrm{d}r \\ &= h - R\left\{ \frac{h}{R} + \frac{1}{12}\left[\frac{h}{R}\right]^3 + \frac{R}{80}\left[\frac{h}{R}\right]^5 + \ldots. \right\} \approx -\frac{1}{12}\frac{h^3}{R^2}. \end{aligned} \tag{55}$$

Secondly, the bending-related portions of the circumferential normal strains on the outer shell surfaces, where $r = (R + h/2)$, need to be of the same size as the stretching-related portions of these strains; mathematically, this can be expressed, when considering (51), as

$$\frac{1}{R + h/2}\left[u_r^C(\varphi, p) + \frac{\mathrm{d}u_\varphi^C(\varphi, p)}{\mathrm{d}\varphi}\right] \approx -\frac{h/2}{R^2 + Rh/2}\left[\frac{\mathrm{d}^2 u_r^C(\varphi, p)}{\mathrm{d}\varphi^2} - \frac{\mathrm{d}u_\varphi^C(\varphi, p)}{\mathrm{d}\varphi}\right]. \tag{56}$$

Given in addition that

$$\left|\frac{1}{R + h/2}\right| \gg \left|\frac{h/2}{R^2 + Rh/2}\right|, \tag{57}$$

(56) readily implies that

$$\left|u_r^C(\varphi, p) + \frac{\mathrm{d}u_\varphi^C(\varphi, p)}{\mathrm{d}\varphi}\right| \ll \left|\frac{\mathrm{d}^2 u_r^C(\varphi, p)}{\mathrm{d}\varphi^2} - \frac{\mathrm{d}u_\varphi^C(\varphi, p)}{\mathrm{d}\varphi}\right| \tag{58}$$

so that only the terms $\mathrm{d}^2 u_r^C/\mathrm{d}\varphi^2$ and $\mathrm{d}u_\varphi^C/\mathrm{d}\varphi$ are not negligible in the expression for the bending moment according to the last line of (54).

As a first step to obtain mathematical solutions for the differential equations (52) and (54), (52) is solved for $\mathrm{d}u_\varphi^C/\mathrm{d}\varphi$, yielding

$$\frac{\mathrm{d}u_\varphi^C(\varphi, p)}{\mathrm{d}\varphi} = \frac{n_\varphi(\varphi, p)}{R_{\mathrm{ax}}^{\mathrm{shell}}(\xi, p)}\frac{R}{h} - u_r^C(\varphi, p). \tag{59}$$

This equation is then re-inserted into (54), yielding a differential equation for u_r^C only. The latter reads as

$$u_r^C(\varphi, p) + \frac{\mathrm{d}^2 u_r^C(\varphi, p)}{\mathrm{d}\varphi^2} - \frac{n_\varphi(\varphi, p)}{R_{\mathrm{ax}}^{\mathrm{shell}}(\xi, p)}\frac{R}{h} + \frac{m_\varphi(\varphi, p)}{R_{\mathrm{ax}}^{\mathrm{shell}}(\xi, p)}\frac{12R^2}{h^3} = 0. \tag{60}$$

Finally, an expression for the angular rotation angle θ_z^C along the circumferential coordinate $\bar{\varphi}$ is derived. Given the small actual deformations, this rotational angle can be approximated by temporal integration over constant angular velocities which are formally identical to the virtual angular velocities introduced in Eq. (9) and right above this equation. They fall into rotational portions associated with the origin and the shell center surface, reading as $\hat{v}_\varphi^C/R$ and $(d\hat{v}_r^C/d\varphi)/R$, so that the rotational angle of the shell generator line positioned at coordinate φ can be expressed in terms of radial and circumferential displacement components as

$$\theta_z^C = \frac{1}{R}\frac{\mathrm{d}u_r^C}{\mathrm{d}\varphi} - \frac{u_\varphi^C}{R}. \tag{61}$$

The solution of the differential equations (59) and (60) for the axial forces (32) and the bending moments (33), as well of Eq. (61) yields an expression for the radial and circumferential displacements of the center surface and the rotational angle of the shell generator. The determination of the three integration constants is done with $u_{r,b}^C = u_r^C(\bar{\varphi} = 0)$ and $u_{\varphi,b}^C = u_\varphi^C(\bar{\varphi} = 0)$; which denotes the radial and circumferential displacements of the center surface at the beginning of the tunnel shell segment, and with $\theta_{z,b}^C = \theta_z^C(\bar{\varphi} = 0)$; which denotes the rotational angle of the shell generator line around an axis oriented in $\mathbf{e}_z$-direction and positioned in the shell center, at the beginning of the tunnel shell segment.

The solution of the differential equation (60) for the axial forces (32) and the bending moments (33), and with the considered integration constants yields

$$
\begin{aligned}
u_r^C(\xi,\bar{\varphi},p) = {} & +u_{r,b}^C(p)\cos(\bar{\varphi}) + u_{\varphi,b}^C(p)\sin(\bar{\varphi}) + R\theta_{z,b}^C(p)\sin(\bar{\varphi}) \\
& + \frac{N_p(p)}{R_{\mathrm{ax}}^{\mathrm{shell}}(\xi,p)}\left\{\frac{12R^3}{h^3}\left[\cos(\bar{\varphi})-1\right] + \left[\frac{R}{2h}+\frac{6R^3}{h^3}\right]\left[\frac{\bar{\varphi}\cos(\bar{\varphi})}{\tan(\Delta\varphi)}\right.\right. \\
& \left.\left. + \bar{\varphi}\sin(\bar{\varphi}) - \frac{\sin(\bar{\varphi})}{\tan(\Delta\varphi)} + \frac{\sin(\bar{\varphi})}{\sin(\Delta\varphi)} - \frac{\bar{\varphi}\cos(\bar{\varphi})}{\sin(\Delta\varphi)}\right]\right\} \\
& + \frac{G_{p,1}(p)}{R_{\mathrm{ax}}^{\mathrm{shell}}(\xi,p)}\left\{\left[\frac{R^2}{h}+\frac{12R^4}{h^3}\right]\left[-1 - \frac{54\bar{\varphi}}{(\Delta\varphi)^3} + \frac{9\bar{\varphi}^3}{2(\Delta\varphi)^3} + \frac{36}{(\Delta\varphi)^2}\right.\right. \\
& - \frac{9\bar{\varphi}^2}{(\Delta\varphi)^2} + \frac{11\bar{\varphi}}{2\Delta\varphi} + \cos(\bar{\varphi}) - \frac{36\cos(\bar{\varphi})}{(\Delta\varphi)^2} \\
& + \frac{\bar{\varphi}\cos(\bar{\varphi})}{2\tan(\Delta\varphi)} - \frac{9\bar{\varphi}\cos(\bar{\varphi})}{(\Delta\varphi)^2\tan(\Delta\varphi)} - \frac{9\bar{\varphi}\cos(\bar{\varphi})}{2(\Delta\varphi)^2\sin(\Delta\varphi)} \\
& + \frac{\bar{\varphi}\sin(\bar{\varphi})}{2} + \frac{54\sin(\bar{\varphi})}{(\Delta\varphi)^3} - \frac{9\bar{\varphi}\sin(\bar{\varphi})}{(\Delta\varphi)^2} - \frac{11\sin(\bar{\varphi})}{2\Delta\varphi} \\
& \left.\left. - \frac{\sin(\bar{\varphi})}{2\tan(\Delta\varphi)} + \frac{9\sin(\bar{\varphi})}{(\Delta\varphi)^2\tan(\Delta\varphi)} + \frac{9\sin(\bar{\varphi})}{2(\Delta\varphi)^2\sin(\Delta\varphi)}\right]\right\} \\
& + \frac{G_{p,2}(p)}{R_{\mathrm{ax}}^{\mathrm{shell}}(\xi,p)}\left\{\left[\frac{R^2}{h}+\frac{12R^4}{h^3}\right]\left[\frac{162\bar{\varphi}}{(\Delta\varphi)^3} - \frac{27\bar{\varphi}^3}{2(\Delta\varphi)^3} - \frac{90}{(\Delta\varphi)^2}\right.\right. \\
& + \frac{45\bar{\varphi}^2}{2(\Delta\varphi)^2} - \frac{9\bar{\varphi}}{\Delta\varphi} + \frac{90\cos(\bar{\varphi})}{(\Delta\varphi)^2} + \frac{45\bar{\varphi}\cos(\bar{\varphi})}{2(\Delta\varphi)^2\tan(\Delta\varphi)} \\
& + \frac{18\bar{\varphi}\cos(\bar{\varphi})}{(\Delta\varphi)^2\sin(\Delta\varphi)} - \frac{162\sin(\bar{\varphi})}{(\Delta\varphi)^3} + \frac{45\bar{\varphi}\sin(\bar{\varphi})}{2(\Delta\varphi)^2} \\
& \left.\left. + \frac{9\sin(\bar{\varphi})}{\Delta\varphi} - \frac{45\sin(\bar{\varphi})}{2(\Delta\varphi)^2\tan(\Delta\varphi)} - \frac{18\sin(\bar{\varphi})}{(\Delta\varphi)^2\sin(\Delta\varphi)}\right]\right\} \\
& + \frac{G_{p,3}(p)}{R_{\mathrm{ax}}^{\mathrm{shell}}(\xi,p)}\left\{\left[\frac{R^2}{h}+\frac{12R^4}{h^3}\right]\left[-\frac{162\bar{\varphi}}{(\Delta\varphi)^3} + \frac{27\bar{\varphi}^3}{2(\Delta\varphi)^3} + \frac{72}{(\Delta\varphi)^2}\right.\right. \\
& - \frac{18\bar{\varphi}^2}{(\Delta\varphi)^2} + \frac{9\bar{\varphi}}{2\Delta\varphi} - \frac{72\cos(\bar{\varphi})}{(\Delta\varphi)^2} - \frac{18\bar{\varphi}\cos(\bar{\varphi})}{(\Delta\varphi)^2\tan(\Delta\varphi)} \\
& - \frac{45\bar{\varphi}\cos(\bar{\varphi})}{2(\Delta\varphi)^2\sin(\Delta\varphi)} + \frac{162\sin(\bar{\varphi})}{(\Delta\varphi)^3} - \frac{18\bar{\varphi}\sin(\bar{\varphi})}{(\Delta\varphi)^2} \\
& \left.\left. - \frac{9\sin(\bar{\varphi})}{2\Delta\varphi} + \frac{18\sin(\bar{\varphi})}{(\Delta\varphi)^2\tan(\Delta\varphi)} + \frac{45\sin(\bar{\varphi})}{2(\Delta\varphi)^2\sin(\Delta\varphi)}\right]\right\} \\
& + \frac{G_{p,4}(p)}{R_{\mathrm{ax}}^{\mathrm{shell}}(\xi,p)}\left\{\left[\frac{R^2}{h}+\frac{12R^4}{h^3}\right]\left[\frac{54\bar{\varphi}}{(\Delta\varphi)^3} - \frac{9\bar{\varphi}^3}{2(\Delta\varphi)^3} - \frac{18}{(\Delta\varphi)^2}\right.\right. \\
& + \frac{9\bar{\varphi}^2}{2(\Delta\varphi)^2} - \frac{\bar{\varphi}}{\Delta\varphi} + \frac{18\cos(\bar{\varphi})}{(\Delta\varphi)^2} + \frac{9\bar{\varphi}\cos(\bar{\varphi})}{2(\Delta\varphi)^2\tan(\Delta\varphi)} \\
& + \frac{9\bar{\varphi}\cos(\bar{\varphi})}{(\Delta\varphi)^2\sin(\Delta\varphi)} - \frac{54\sin(\bar{\varphi})}{(\Delta\varphi)^3} + \frac{9\bar{\varphi}\sin(\bar{\varphi})}{2(\Delta\varphi)^2} - \frac{\bar{\varphi}\cos(\bar{\varphi})}{2\sin(\Delta\varphi)} \\
& \left.\left. + \frac{\sin(\bar{\varphi})}{\Delta\varphi} - \frac{9\sin(\bar{\varphi})}{2(\Delta\varphi)^2\tan(\Delta\varphi)} + \frac{\sin(\bar{\varphi})}{2\sin(\Delta\varphi)} - \frac{9\sin(\bar{\varphi})}{(\Delta\varphi)^2\sin(\Delta\varphi)}\right]\right\}.
\end{aligned}
\tag{62}
$$

We explicitly note the interesting structure of the force-driven portion of the solution for the radial displacements (62), which, when remembering (49.1), can be written as the product of the uniaxial creep function $J(\xi, p)$ with the ground/impost pressure-weighted sum of time-invariant influence functions $\mathcal{I}$, depending on ν, R, h, and $\bar{\varphi}$; according to

$$\begin{aligned} &u_r^C(\xi,\bar{\varphi},p) - u_{r,b}^C(p)\cos(\bar{\varphi}) - u_{\varphi,b}^C(p)\sin(\bar{\varphi}) - R\theta_{z,b}^C(p)\sin(\bar{\varphi}) \\ &\quad = J(\xi,p)\left\{N_p(p)\,\mathcal{I}_{N\to r}(\bar{\varphi}) + \sum_{i=1}^{4}\left[G_{p,i}(p)\,\mathcal{I}_{i\to r}(\bar{\varphi})\right]\right\} \end{aligned} \tag{63}$$

with the traction-to-displacement influence functions $\mathcal{I}$ given as Eqs. (99)–(103) in Appendix B. Back-transformation of (63) to the time domain according to

$$f(t) = \frac{1}{2\pi i}\int_{\gamma-i\infty}^{\gamma+i\infty} f(p)\exp(pt)\,\mathrm{d}p \tag{64}$$

yields

$$\begin{aligned} &u_r^C(\xi,\bar{\varphi},t) - u_{r,b}^C(t)\cos(\bar{\varphi}) - u_{\varphi,b}^C(t)\sin(\bar{\varphi}) - R\theta_{z,b}^C(t)\sin(\bar{\varphi}) \\ &\quad = +\mathcal{I}_{N\to r}(\bar{\varphi})\int_0^t J(t-\tau)\dot{N}_p(\tau)\,\mathrm{d}\tau + \sum_{i=1}^{4}\left[\mathcal{I}_{i\to r}(\bar{\varphi})\int_0^t J(t-\tau)\dot{G}_{p,i}(\tau)\,\mathrm{d}\tau\right]. \end{aligned} \tag{65}$$

The solution of the differential equation (59) for the axial forces (32) and the radial displacements (62), and with the considered integration constants yields

$$\begin{aligned} u_\varphi^C(\xi,\bar{\varphi},p) = &-u_{r,b}^C(p)\sin(\bar{\varphi}) + u_{\varphi,b}^C(p)\cos(\bar{\varphi}) + R\theta_{z,b}^C(p)\{\cos(\bar{\varphi})-1\} \\ &+\frac{N_p(p)}{R_{\mathrm{ax}}^{\mathrm{shell}}(\xi,p)}\left\{\left[\frac{R}{2h}+\frac{6R^3}{h^3}\right]\left[+\bar{\varphi}\cos(\bar{\varphi}) - 3\sin(\bar{\varphi})\right.\right. \\ &\left.-\frac{\bar{\varphi}\sin(\bar{\varphi})}{\tan(\Delta\varphi)}+\frac{\bar{\varphi}\sin(\bar{\varphi})}{\sin(\Delta\varphi)}\right]+\frac{R}{h}\left[+2\sin(\bar{\varphi})\right] \\ &\left.+\frac{12R^3}{h^3}\left[+\bar{\varphi}-\frac{\cos(\bar{\varphi})-1}{\tan(\Delta\varphi)}+\frac{\cos(\bar{\varphi})-1}{\sin(\Delta\varphi)}\right]\right\} \\ &+\frac{G_{p,1}(p)}{R_{\mathrm{ax}}^{\mathrm{shell}}(\xi,p)}\left\{\left[\frac{R^2}{h}+\frac{12R^4}{h^3}\right]\left[-\frac{54-54\cos(\bar{\varphi})}{(\Delta\varphi)^3}+\frac{11-11\cos(\bar{\varphi})}{2\Delta\varphi}\right.\right. \\ &+\frac{\bar{\varphi}\cos(\bar{\varphi})}{2}-\frac{9\bar{\varphi}\cos(\bar{\varphi})}{(\Delta\varphi)^2}-\frac{\bar{\varphi}\sin(\bar{\varphi})}{2\tan(\Delta\varphi)}+\frac{9\bar{\varphi}\sin(\bar{\varphi})}{(\Delta\varphi)^2\tan(\Delta\varphi)} \\ &\left.+\frac{9\bar{\varphi}\sin(\bar{\varphi})}{2(\Delta\varphi)^2\sin(\Delta\varphi)}\right]+\frac{R^2}{h}\left[+\frac{27\bar{\varphi}^2}{2(\Delta\varphi)^3}-\frac{18\bar{\varphi}}{(\Delta\varphi)^2}-\frac{\sin(\bar{\varphi})}{2}\right. \\ &\left.+\frac{27\sin(\bar{\varphi})}{(\Delta\varphi)^2}\right]+\frac{12R^4}{h^3}\left[\frac{3\bar{\varphi}^3}{(\Delta\varphi)^2}-\frac{9\bar{\varphi}^4}{8(\Delta\varphi)^3}-\frac{11\bar{\varphi}^2}{4\Delta\varphi}\right. \\ &+\frac{27\bar{\varphi}^2}{(\Delta\varphi)^3}-\frac{36\bar{\varphi}}{(\Delta\varphi)^2}-\frac{3\sin(\bar{\varphi})}{2}+\frac{45\sin(\bar{\varphi})}{(\Delta\varphi)^2} \\ &\left.\left.-\frac{9-9\cos(\bar{\varphi})}{(\Delta\varphi)^2\sin(\Delta\varphi)}+\frac{1-\cos(\bar{\varphi})}{\tan(\Delta\varphi)}-\frac{18-18\cos(\bar{\varphi})}{(\Delta\varphi)^2\tan(\Delta\varphi)}+\bar{\varphi}\right]\right\} \\ &+\frac{G_{p,2}(p)}{R_{\mathrm{ax}}^{\mathrm{shell}}(\xi,p)}\left\{\left[\frac{R^2}{h}+\frac{12R^4}{h^3}\right]\left[+\frac{162-162\cos(\bar{\varphi})}{(\Delta\varphi)^3}-\frac{9-9\cos(\bar{\varphi})}{\Delta\varphi}\right.\right. \\ &\left.\left.-\frac{45\bar{\varphi}\sin(\bar{\varphi})}{2(\Delta\varphi)^2\tan(\Delta\varphi)}-\frac{18\bar{\varphi}\sin(\bar{\varphi})}{(\Delta\varphi)^2\sin(\Delta\varphi)}+\frac{45\bar{\varphi}\cos(\bar{\varphi})}{2(\Delta\varphi)^2}\right]\right. \end{aligned}$$

$$
\begin{aligned}
&+\frac{12R^4}{h^3}\Bigg[-\frac{81\bar{\varphi}^2}{(\Delta\varphi)^3}+\frac{27\bar{\varphi}^4}{8(\Delta\varphi)^3}+\frac{90\bar{\varphi}}{(\Delta\varphi)^2}-\frac{15\bar{\varphi}^3}{2(\Delta\varphi)^2}\\
&+\frac{9\bar{\varphi}^2}{2\Delta\varphi}+\frac{45-45\cos(\bar{\varphi})}{(\Delta\varphi)^2\tan(\Delta\varphi)}+\frac{36-36\cos(\bar{\varphi})}{(\Delta\varphi)^2\sin(\Delta\varphi)}\\
&-\frac{225\sin(\bar{\varphi})}{2(\Delta\varphi)^2}\Bigg]+\frac{R^2}{h}\Bigg[-\frac{81\bar{\varphi}^2}{2(\Delta\varphi)^3}+\frac{45\bar{\varphi}}{(\Delta\varphi)^2}-\frac{135\sin(\bar{\varphi})}{2(\Delta\varphi)^2}\Bigg]\Bigg\}\\
&+\frac{G_{p,3}(p)}{R_{\mathrm{ax}}^{\mathrm{shell}}(\xi,\,p)}\Bigg\{\Bigg[\frac{R^2}{h}+\frac{12R^4}{h^3}\Bigg]\Bigg[-\frac{162-162\cos(\bar{\varphi})}{(\Delta\varphi)^3}+\frac{9-9\cos(\bar{\varphi})}{2\Delta\varphi}\\
&-\frac{18\bar{\varphi}\cos(\bar{\varphi})}{(\Delta\varphi)^2}+\frac{18\bar{\varphi}\sin(\bar{\varphi})}{(\Delta\varphi)^2\tan(\Delta\varphi)}+\frac{45\bar{\varphi}\sin(\bar{\varphi})}{2(\Delta\varphi)^2\sin(\Delta\varphi)}\Bigg]\\
&+\frac{12R^4}{h^3}\Bigg[\frac{81\bar{\varphi}^2}{(\Delta\varphi)^3}-\frac{27\bar{\varphi}^4}{8(\Delta\varphi)^3}-\frac{72\bar{\varphi}}{(\Delta\varphi)^2}+\frac{6\bar{\varphi}^3}{(\Delta\varphi)^2}\\
&-\frac{9\bar{\varphi}^2}{4\Delta\varphi}-\frac{36-36\cos(\bar{\varphi})}{(\Delta\varphi)^2\tan(\Delta\varphi)}-\frac{45-45\cos(\bar{\varphi})}{(\Delta\varphi)^2\sin(\Delta\varphi)}\\
&+\frac{90\sin(\bar{\varphi})}{(\Delta\varphi)^2}\Bigg]+\frac{R^2}{h}\Bigg[\frac{81\bar{\varphi}^2}{2(\Delta\varphi)^3}-\frac{36\bar{\varphi}}{(\Delta\varphi)^2}+\frac{54\sin(\bar{\varphi})}{(\Delta\varphi)^2}\Bigg]\Bigg\}\\
&+\frac{G_{p,4}(p)}{R_{\mathrm{ax}}^{\mathrm{shell}}(\xi,\,p)}\Bigg\{\Bigg[\frac{R^2}{h}+\frac{12R^4}{h^3}\Bigg]\Bigg[-\frac{1}{\Delta\varphi}+\frac{54-54\cos(\bar{\varphi})}{\Delta\varphi^3}+\frac{9\bar{\varphi}\cos(\bar{\varphi})}{2\Delta\varphi^2}\\
&-\frac{9\bar{\varphi}\sin(\bar{\varphi})}{2\Delta\varphi^2\tan(\Delta\varphi)}+\frac{\bar{\varphi}\sin(\bar{\varphi})}{2\sin(\Delta\varphi)}-\frac{9\bar{\varphi}\sin(\bar{\varphi})}{\Delta\varphi^2\sin(\Delta\varphi)}\\
&+\frac{\cos(\bar{\varphi})}{\Delta\varphi}\Bigg]+\frac{12R^4}{h^3}\Bigg[-\frac{27\bar{\varphi}^2}{\Delta\varphi^3}+\frac{9\bar{\varphi}^4}{8\Delta\varphi^3}+\frac{18\bar{\varphi}}{\Delta\varphi^2}-\frac{3\bar{\varphi}^3}{2\Delta\varphi^2}\\
&+\frac{\bar{\varphi}^2}{2\Delta\varphi}-\frac{45\sin(\bar{\varphi})}{2\Delta\varphi^2}+\frac{9-9\cos(\bar{\varphi})}{\Delta\varphi^2\tan(\Delta\varphi)}-\frac{1-\cos(\bar{\varphi})}{\sin(\Delta\varphi)}\\
&+\frac{18-18\cos(\bar{\varphi})}{\Delta\varphi^2\sin(\Delta\varphi)}\Bigg]+\frac{R^2}{h}\Bigg[+\frac{9\bar{\varphi}}{\Delta\varphi^2}-\frac{27\bar{\varphi}^2}{2\Delta\varphi^3}-\frac{27\sin(\bar{\varphi})}{2\Delta\varphi^2}\Bigg]\Bigg\}. \qquad (66)
\end{aligned}
$$

In analogy to (63), this expression can be written in terms of polar angle-specific influence functions, resulting in the following relation after transformation into the time domain:

$$
\begin{aligned}
&u_{\varphi}^{C}(\xi,\bar{\varphi},t)+u_{r,b}^{C}(t)\sin(\bar{\varphi})-u_{\varphi,b}^{C}(t)\cos(\bar{\varphi})-R\theta_{z,b}^{C}(t)\{\cos(\bar{\varphi})-1\}\\
&\quad=+\mathcal{I}_{N\to\varphi}(\bar{\varphi})\int_0^t J(t-\tau)\dot{N}_p(\tau)\,\mathrm{d}\tau\\
&\quad\quad+\sum_{i=1}^{4}\Bigg[\mathcal{I}_{i\to\varphi}(\bar{\varphi})\int_0^t J(t-\tau)\dot{G}_{p,i}(\tau)\,\mathrm{d}\tau\Bigg] \qquad (67)
\end{aligned}
$$

with the influence functions $\mathcal{I}$ given as Eqs. (104)–(108) in Appendix B. The final mathematical solution for the rotational angle of the shell generator yields

$$
\begin{aligned}
\theta_z^C(\xi,\bar{\varphi},p)=&+\theta_{z,b}^{C}(p)+\frac{G_{p,1}(p)}{R_{\mathrm{ax}}^{\mathrm{shell}}(\xi,\,p)}\Bigg\{\frac{12R^3}{h^3}\Bigg[-\bar{\varphi}-\frac{27\bar{\varphi}^2}{2(\Delta\varphi)^3}+\frac{9\bar{\varphi}^4}{8(\Delta\varphi)^3}+\frac{18\bar{\varphi}}{(\Delta\varphi)^2}\\
&-\frac{3\bar{\varphi}^3}{(\Delta\varphi)^2}+\frac{11\bar{\varphi}^2}{4\Delta\varphi}-\frac{1-\cos(\bar{\varphi})}{\tan(\Delta\varphi)}+\sin(\bar{\varphi})\\
&-\frac{18\sin(\bar{\varphi})}{(\Delta\varphi)^2}+\frac{18-18\cos(\bar{\varphi})}{(\Delta\varphi)^2\tan(\Delta\varphi)}+\frac{9-9\cos(\bar{\varphi})}{(\Delta\varphi)^2\sin(\Delta\varphi)}\Bigg]\Bigg\}\\
&+\frac{G_{p,2}(p)}{R_{\mathrm{ax}}^{\mathrm{shell}}(\xi,\,p)}\Bigg\{\frac{12R^3}{h^3}\Bigg[+\frac{81\bar{\varphi}^2}{2(\Delta\varphi)^3}-\frac{27\bar{\varphi}^4}{8(\Delta\varphi)^3}-\frac{45\bar{\varphi}}{(\Delta\varphi)^2}+\frac{15\bar{\varphi}^3}{2(\Delta\varphi)^2}
\end{aligned}
$$

$$
\begin{aligned}
&-\frac{9\bar{\varphi}^2}{2\Delta\varphi}+\frac{45\sin(\bar{\varphi})}{(\Delta\varphi)^2}-\frac{45-45\cos(\bar{\varphi})}{(\Delta\varphi)^2\tan(\Delta\varphi)}-\frac{36-36\cos(\bar{\varphi})}{(\Delta\varphi)^2\sin(\Delta\varphi)}\Bigg]\Bigg\}\\
&+\frac{G_{p,3}(p)}{R_{\mathrm{ax}}^{\mathrm{shell}}(\xi,\,p)}\Bigg\{\frac{12R^3}{h^3}\Bigg[-\frac{81\bar{\varphi}^2}{2(\Delta\varphi)^3}+\frac{27\bar{\varphi}^4}{8(\Delta\varphi)^3}+\frac{36\bar{\varphi}}{(\Delta\varphi)^2}-\frac{6\bar{\varphi}^3}{(\Delta\varphi)^2}\\
&+\frac{9\bar{\varphi}^2}{4\Delta\varphi}-\frac{36\sin(\bar{\varphi})}{(\Delta\varphi)^2}+\frac{36-36\cos(\bar{\varphi})}{(\Delta\varphi)^2\tan(\Delta\varphi)}+\frac{45-45\cos(\bar{\varphi})}{(\Delta\varphi)^2\sin(\Delta\varphi)}\Bigg]\Bigg\}\\
&+\frac{G_{p,4}(p)}{R_{\mathrm{ax}}^{\mathrm{shell}}(\xi,\,p)}\Bigg\{\frac{12R^3}{h^3}\Bigg[+\frac{27\bar{\varphi}^2}{2(\Delta\varphi)^3}-\frac{9\bar{\varphi}^4}{8(\Delta\varphi)^3}-\frac{9\bar{\varphi}}{(\Delta\varphi)^2}\\
&+\frac{3\bar{\varphi}^3}{2(\Delta\varphi)^2}-\frac{\bar{\varphi}^2}{2\Delta\varphi}+\frac{9\sin(\bar{\varphi})}{(\Delta\varphi)^2}\\
&-\frac{9-9\cos(\bar{\varphi})}{(\Delta\varphi)^2\tan(\Delta\varphi)}-\frac{18-18\cos(\bar{\varphi})}{(\Delta\varphi)^2\sin(\Delta\varphi)}+\frac{1-\cos(\bar{\varphi})}{\sin(\Delta\varphi)}\Bigg]\Bigg\}\\
&+\frac{N_p(p)}{R_{\mathrm{ax}}^{\mathrm{shell}}(\xi,\,p)}\Bigg\{\frac{12R^2}{h^3}\Bigg[\frac{\cos(\bar{\varphi})-1}{\tan(\Delta\varphi)}+\frac{1-\cos(\bar{\varphi})}{\sin(\Delta\varphi)}+\sin(\bar{\varphi})-\bar{\varphi}\Bigg]\Bigg\}. \qquad (68)
\end{aligned}
$$

In analogy to (63), this expression can be written in terms of polar angle-specific influence functions, resulting in the following relation after transformation into the time domain:

$$
\begin{aligned}
\theta_z^C(\xi,\bar{\varphi},t)-\theta_{z,b}^C(t) = &+\mathcal{I}_{N\to z}(\bar{\varphi})\int_0^t J(t-\tau)\dot{N}_p(\tau)\,\mathrm{d}\tau\\
&+\sum_{i=1}^{4}\Bigg[\mathcal{I}_{i\to z}(\bar{\varphi})\int_0^t J(t-\tau)\dot{G}_{p,i}(\tau)\,\mathrm{d}\tau\Bigg] \qquad (69)
\end{aligned}
$$

with the influence functions $\mathcal{I}$ given as Eqs. (109)–(113) in Appendix B.

3.3 Aging and nonlinear creep—degree of utilization

Equations (65), (67), and (69) quantify the creep behavior of the entire shotcrete tunnel shell, in terms of displacements and cross-sectional rotations as functions of ground and impost pressures, for a constant degree of hydration. However, the latter itself evolves with time as well. Hence, the aforementioned relations, strictly speaking, are only valid for a very short time interval during which the hydration degree is actually constant. Accordingly, adopting the experimentally validated conceptual reasoning outlined in [28], we apply these creep relations in rate form, for each and every time instant and the then prevailing degree of hydration. Differentiation of the corresponding parameter integrals results in

$$
\begin{aligned}
&\dot{u}_r^C(\xi,\bar{\varphi},t)-\dot{u}_{r,b}^C(t)\cos(\bar{\varphi})-\dot{u}_{\varphi,b}^C(t)\sin(\bar{\varphi})-R\dot{\theta}_{z,b}^C(t)\sin(\bar{\varphi})\\
&\quad=+\mathcal{I}_{N\to r}(\bar{\varphi})\Bigg[\frac{\dot{N}_p(t)}{E\big(\xi(t)\big)}+\int_0^t\frac{\partial J}{\partial t}\big(\xi(t),t-\tau\big)\dot{N}_p(\tau)\,\mathrm{d}\tau\Bigg]\\
&\qquad+\sum_{i=1}^{4}\Bigg\{\mathcal{I}_{i\to r}(\bar{\varphi})\Bigg[\frac{\dot{G}_{p,i}(t)}{E\big(\xi(t)\big)}+\int_0^t\frac{\partial J}{\partial t}\big(\xi(t),t-\tau\big)\dot{G}_{p,i}(\tau)\,\mathrm{d}\tau\Bigg]\Bigg\} \qquad (70)
\end{aligned}
$$

whereby we made use of $J\big(\xi(t),0\big)=1/E\big(\xi(t)\big)$ according to Eq. (39). In analogy to (70), the rate forms for the circumferential displacements and the rotational angles around $\mathbf{e}_z$ read as

$$
\begin{aligned}
&\dot{u}_\varphi^C(\xi,\bar{\varphi},t)+\dot{u}_{r,b}^C(t)\sin(\bar{\varphi})-\dot{u}_{\varphi,b}^C(t)\cos(\bar{\varphi})-R\dot{\theta}_{z,b}^C(t)\,\{\cos(\bar{\varphi})-1\}\\
&\quad=+\mathcal{I}_{N\to\varphi}(\bar{\varphi})\Bigg[\frac{\dot{N}_p(t)}{E\big(\xi(t)\big)}+\int_0^t\frac{\partial J}{\partial t}\big(\xi(t),t-\tau\big)\dot{N}_p(\tau)\,\mathrm{d}\tau\Bigg]\\
&\qquad+\sum_{i=1}^{4}\Bigg\{\mathcal{I}_{i\to\varphi}(\bar{\varphi})\Bigg[\frac{\dot{G}_{p,i}(t)}{E\big(\xi(t)\big)}+\int_0^t\frac{\partial J}{\partial t}\big(\xi(t),t-\tau\big)\dot{G}_{p,i}(\tau)\,\mathrm{d}\tau\Bigg]\Bigg\} \qquad (71)
\end{aligned}
$$

and

$$\begin{aligned}\dot{\theta}_z^C(\xi,\bar{\varphi},t)-\dot{\theta}_{z,b}^C(t)&\\ =+\mathcal{I}_{N\to z}(\bar{\varphi})\left[\frac{\dot{N}_p(t)}{E\big(\xi(t)\big)}+\int_0^t\frac{\partial J}{\partial t}\big(\xi(t),t-\tau\big)\dot{N}_p(\tau)\,\mathrm{d}\tau\right]&\\ +\sum_{i=1}^{4}\left\{\mathcal{I}_{i\to z}(\bar{\varphi})\left[\frac{\dot{G}_{p,i}(t)}{E\big(\xi(t)\big)}+\int_0^t\frac{\partial J}{\partial t}\big(\xi(t),t-\tau\big)\dot{G}_{p,i}(\tau)\,\mathrm{d}\tau\right]\right\}.&\end{aligned}\tag{72}$$

Finally, it is known that the creep compliance increases nonlinearly with the stress once a critical load level is exceeded. This is elegantly quantified in terms of the affinity concept of Ruiz et al [25], according to which the rate of the creep function (39) needs to be multiplied by a factor η,

$$\frac{\partial J^{\mathrm{NL}}}{\partial t}=\eta\,\frac{\partial J}{\partial t},\tag{73}$$

with the affinity factor reading as

$$\eta=1+2\mathcal{L}^4\quad\text{for}\quad\mathcal{L}>0\tag{74}$$

whereby $\mathcal{L}$ is the level of loading associated with the strength of the material. In the line of [38], $\mathcal{L}$ is associated with a Drucker-Prager strength criterion applied to the stresses at the center line of the tunnel shell, so that

$$\begin{aligned}\mathcal{L}(\bar{\varphi},t)=+\frac{\alpha_{\mathrm{DP}}}{k_{\mathrm{DP}}}\Big[\sigma_{\varphi\varphi}(r=R,\bar{\varphi},t)+\sigma_{zz}(r=R,\bar{\varphi},t)\Big]&\\ +\frac{1}{k_{\mathrm{DP}}}\left\{\left[+\frac{2}{3}\sigma_{\varphi\varphi}(r=R,\bar{\varphi},t)-\frac{1}{3}\sigma_{zz}(r=R,\bar{\varphi},t)\right]^2\right.&\\ +\left[-\frac{1}{3}\sigma_{\varphi\varphi}(r=R,\bar{\varphi},t)-\frac{1}{3}\sigma_{zz}(r=R,\bar{\varphi},t)\right]^2&\\ \left.+\left[-\frac{1}{3}\sigma_{\varphi\varphi}(r=R,\bar{\varphi},t)+\frac{2}{3}\sigma_{zz}(r=R,\bar{\varphi},t)\right]^2\right\}^{0.5}&\end{aligned}\tag{75}$$

with parameters α_{DP} and k_{DP} being related to the uniaxial and biaxial compressive strengths f_c and f_b of shotcrete,

$$\alpha_{\mathrm{DP}}=\sqrt{\frac{2}{3}}\frac{\kappa-1}{2\kappa-1};\quad k_{\mathrm{DP}}=\sqrt{\frac{2}{3}}\left[1-\frac{\kappa-1}{2\kappa-1}\right]f_c;\quad\kappa=\frac{f_b}{f_c}\tag{76}$$

where $\kappa=1.15$ follows from standard tests [15], and f_c follows the evolution given by Eq. (35). We note that the format of (74) maintains the consideration of homogeneous creep properties, as introduced in Eq. (50.2).

4 Application to a benchmark example: Sieberg tunnel

4.1 Geometrical and material properties

The analytical mechanics model for an aging viscoelastic cylindrical shell segment, as developed in Sects. 2 and 3, is eventually applied to a benchmark example in NATM tunneling, which has been analyzed by various types of "hybrid methods" combining geodetic measurements with material and structural mechanics tools [11,12,36–38]: This benchmark example is built on cross section MC1452 of the Sieberg tunnel, a tunnel constructed in the 1990s as part of the high-speed railway line connecting Vienna and Salzburg. In terms of the geometrical properties introduced in Sects. 2 and 3, it is characterized by radius $R=6.20$ m, a thickness $h=0.30$ m, and an opening angle $\Delta\varphi=2.92$ rad $=167.30°$, see Fig. 6. During the top heading excavation and installation stage, it was equipped with three optical reflectors delivering displacement vectors in three measurement points (MPs), MP1, MP2, and MP3, see Fig. 6; and we here consider the corresponding measurements over the first 28 days of the lifetime of the Sieberg tunnel, see Table 2. Moreover, we consider a typical shotcrete mixture with the cement type CEM II/A-S 42.5R, effective water-to-cement mass ratio $(w/c)_{eff}=0.5$, aggregate-to-cement mass ratio $a/c=4.48$, and volume fractions of aggregates $f_{\mathrm{agg}}^{\mathrm{con}}=0.70$. For such a composition, Figures 13 and 3 of [38] suggest the following values for the degree of hydration and uniaxial strength after 28 days of shotcrete age: $\xi=0.8762$ and $f_{c,28\mathrm{d}}=58.14$ MPa.

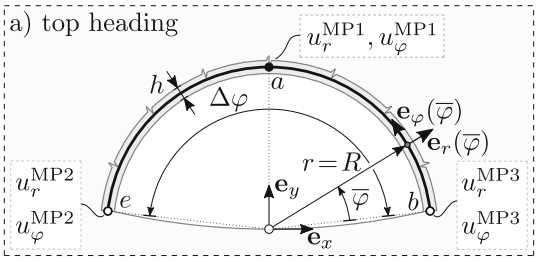

Fig. 6 Top heading of the Sieberg tunnel: definition of $\mathbf{e}_x$-$\mathbf{e}_y$ and $\mathbf{e}_r(\bar{\varphi})$-$\mathbf{e}_\varphi(\bar{\varphi})$ coordinate frames, geometric properties, and locations of measurement points MP1, MP2, and MP3

Table 2 Radial and circumferential displacement components measured (in meters) at three geodetic reflectors installed within cross section MC1452 of the Sieberg tunnel; as seen in Fig. 6

viewing time	Measurement point MP1		Measurement point MP2		Measurement point MP3	
	$u_{r,a}^C = u_r^{\mathrm{MP1}}$	$u_{\varphi,a}^C = u_\varphi^{\mathrm{MP1}}$	$u_{r,e}^C = u_r^{\mathrm{MP2}}$	$u_{\varphi,e}^C = u_\varphi^{\mathrm{MP2}}$	$u_{r,b}^C = u_r^{\mathrm{MP3}}$	$u_{\varphi,b}^C = u_\varphi^{\mathrm{MP3}}$
$t_0 = 0.000$ d	±0.00000	±0.00000	±0.00000	±0.00000	±0.00000	±0.00000
$t_1 = 0.052$ d	−0.00081	+0.00001	−0.00023	+0.00025	−0.00020	−0.00015
$t_2 = 0.120$ d	−0.00185	+0.00002	−0.00054	+0.00056	−0.00047	−0.00034
$t_3 = 0.252$ d	−0.00387	+0.00004	−0.00112	+0.00118	−0.00102	−0.00073
$t_4 = 0.464$ d	−0.00715	+0.00007	−0.00204	+0.00214	−0.00195	−0.00136
$t_5 = 0.792$ d	−0.01177	+0.00013	−0.00346	+0.00374	−0.00359	−0.00241
$t_6 = 1.264$ d	−0.01621	−0.00010	−0.00490	+0.00521	−0.00505	−0.00385
$t_7 = 1.928$ d	−0.01834	−0.00072	−0.00632	+0.00631	−0.00585	−0.00536
$t_8 = 2.824$ d	−0.01989	−0.00017	−0.00768	+0.00740	−0.00471	−0.00662
$t_9 = 4.000$ d	−0.02055	+0.00081	−0.00851	+0.00795	−0.00421	−0.00743
$t_{10} = 5.600$ d	−0.02086	−0.00052	−0.00933	+0.00812	−0.00465	−0.00911
$t_{11} = 6.690$ d	−0.02076	−0.00087	−0.00955	+0.00818	−0.00473	−0.00814
$t_{12} = 7.795$ d	−0.02056	−0.00080	−0.01015	+0.00842	−0.00434	−0.00830
$t_{13} = 10.806$ d	−0.02050	−0.00086	−0.01121	+0.00846	−0.00444	−0.00816
$t_{14} = 14.928$ d	−0.02050	−0.00094	−0.01212	+0.00831	−0.00459	−0.00793
$t_{15} = 20.599$ d	−0.01993	−0.00112	−0.01135	+0.00808	−0.00447	−0.00821
$t_{16} = 24.000$ d	−0.02032	−0.00122	−0.01096	+0.00801	−0.00424	−0.00840
$t_{17} = 25.000$ d	−0.02049	−0.00073	−0.01166	+0.00894	−0.00466	−0.00869
$t_{18} = 26.000$ d	−0.02068	−0.00173	−0.01183	+0.00918	−0.00500	−0.00908
$t_{19} = 27.000$ d	−0.02044	−0.00014	−0.01191	+0.00913	−0.00560	−0.00924
$t_{20} = 28.000$ d	−0.02002	−0.00101	−0.01139	+0.00890	−0.00633	−0.00897

4.2 Displacement-to-force conversion

The conversion of displacements measured in MP1, MP2, and MP3, into compressive traction forces acting on the other shell surfaces and on the imposts is based on a temporally discretized version of Eqs. (70)–(72), along with Eqs. (99)–(113) of Appendix B. Between chosen time instants since the installation of the top heading, see Table 2, the temporal evolutions of the displacements and rotational angles are approximated linearly, so that the corresponding rates become constants during the time intervals $[t_i, t_{i+1}]$, according to

$$\dot{u}_r(\Delta t_{n+1}) = \frac{u_r(t_{n+1}) - u_r(t_n)}{\Delta t_{n+1}} \quad \text{for} \quad t \in [t_n, t_{n+1}], \tag{77}$$

$$\dot{u}_\varphi(\Delta t_{n+1}) = \frac{u_\varphi(t_{n+1}) - u_\varphi(t_n)}{\Delta t_{n+1}} \quad \text{for} \quad t \in [t_n, t_{n+1}], \tag{78}$$

$$\dot{\theta}_z(\Delta t_{n+1}) = \frac{\theta_z(t_{n+1}) - \theta_z(t_n)}{\Delta t_{n+1}} \quad \text{for} \quad t \in [t_n, t_{n+1}] \tag{79}$$

whereby

$$\Delta t_{n+1} = t_{n+1} - t_n. \tag{80}$$

The same temporal approximation type is used for the ground and impost pressure values N_p and $G_{p,i}$, with $i = 1, 2, 3, 4$, according to

$$\dot{N}_p(\Delta t_{n+1}) = \frac{N_p(t_{n+1}) - N_p(t_n)}{\Delta t_{n+1}} \quad \text{for} \quad t \in [t_n, t_{n+1}], \tag{81}$$

$$\dot{G}_{p,i}(\Delta t_{n+1}) = \frac{G_{p,i}(t_{n+1}) - G_{p,i}(t_n)}{\Delta t_{n+1}} \text{ with } i = 1, 2, 3, 4 \text{ for } t \in [t_n, t_{n+1}]. \tag{82}$$

Finally, also the material properties are considered to evolve linearly with time between any two of the instants given in Table 2, so that

$$E(t) = E\big(\xi(t_n)\big) + \frac{t - t_n}{\Delta t_{n+1}}\Big[E\big(\xi(t_{n+1})\big) - E\big(\xi(t_n)\big)\Big] \quad \text{for} \quad t \in [t_n, t_{n+1}], \tag{83}$$

$$\begin{aligned}\frac{\partial J^{\mathrm{NL}}}{\partial t}(t) &= \frac{\partial J^{\mathrm{NL}}}{\partial t}\big(\xi(t_n), t - t_n\big) + \frac{t - t_n}{\Delta t_{n+1}}\Big[\frac{\partial J^{\mathrm{NL}}}{\partial t}\big(\xi(t_{n+1}), t - t_n\big) \\ &\quad - \frac{\partial J^{\mathrm{NL}}}{\partial t}\big(\xi(t_n), t - t_n\big)\Big] \\ &= \eta\left\{\frac{1}{E_c\big(\xi(t_n)\big)} + \frac{t - t_n}{\Delta t_{n+1}}\left[\frac{1}{E_c\big(\xi(t_{n+1})\big)} - \frac{1}{E_c\big(\xi(t_n)\big)}\right]\right\}\frac{\beta}{t_0}\left[\frac{t}{t_0}\right]^{\beta-1}.\end{aligned} \tag{84}$$

Use of (77)–(84) in the rate equations (70)–(72) yields the following discretized format for the increments of radial and circumferential displacements and of rotational angles, respectively,

$$\begin{aligned}&+\frac{u_r^C(\xi, \bar{\varphi}, t_{n+1}) - u_r^C(\xi, \bar{\varphi}, t_n)}{\Delta t_{n+1}} - \frac{u_{r,b}^C(t_{n+1}) - u_{r,b}^C(t_n)}{\Delta t_{n+1}}\Big[\cos(\bar{\varphi})\Big] \\ &-\frac{u_{\varphi,b}^C(t_{n+1}) - u_{\varphi,b}^C(t_n)}{\Delta t_{n+1}}\Big[\sin(\bar{\varphi})\Big] - \frac{R\theta_{z,b}^C(t_{n+1}) - R\theta_{z,b}^C(t_n)}{\Delta t_{n+1}}\Big[\sin(\bar{\varphi})\Big] \\ &= +\mathcal{I}_{N\to r}(\bar{\varphi})\Big[\frac{N_p(t_{n+1}) - N_p(t_n)}{E\big(\xi(t_{n+1})\big)\Delta t_{n+1}} \\ &\quad + \frac{\Delta t_{n+1}}{2}\left(\frac{\partial J^{\mathrm{NL}}}{\partial t}(t_n) + \frac{\partial J^{\mathrm{NL}}}{\partial t}(t_{n+1})\right)\frac{N_p(t_{n+1}) - N_p(t_n)}{\Delta t_{n+1}}\Big] \\ &\quad + \sum_{i=1}^{4}\left\{\mathcal{I}_{i\to r}(\bar{\varphi})\Big[\frac{G_{p,i}(t_{n+1}) - G_{p,i}(t_n)}{E\big(\xi(t_{n+1})\big)\Delta t_{n+1}}\right. \\ &\quad \left. + \frac{\Delta t_{n+1}}{2}\left(\frac{\partial J^{\mathrm{NL}}}{\partial t}(t_n) + \frac{\partial J^{\mathrm{NL}}}{\partial t}(t_{n+1})\right)\frac{G_{p,i}(t_{n+1}) - G_{p,i}(t_n)}{\Delta t_{n+1}}\Big]\right\} \\ &\quad + \frac{u_\varphi^C(\xi, \bar{\varphi}, t_{n+1}) - u_\varphi^C(\xi, \bar{\varphi}, t_n)}{\Delta t_{n+1}} + \frac{u_{r,b}^C(t_{n+1}) - u_{r,b}^C(t_n)}{\Delta t_{n+1}}\Big[\sin(\bar{\varphi})\Big] \\ &\quad - \frac{u_{\varphi,b}^C(t_{n+1}) - u_{\varphi,b}^C(t_n)}{\Delta t_{n+1}}\Big[\cos(\bar{\varphi})\Big] - \frac{R\theta_{z,b}^C(t_{n+1}) - R\theta_{z,b}^C(t_n)}{\Delta t_{n+1}}\Big[\cos(\bar{\varphi}) - 1\Big]\end{aligned} \tag{85}$$

$$\begin{aligned}&= +\mathcal{I}_{N\to\varphi}(\bar{\varphi})\Big[\frac{N_p(t_{n+1}) - N_p(t_n)}{E\big(\xi(t_{n+1})\big)\Delta t_{n+1}} \\ &\quad + \frac{\Delta t_{n+1}}{2}\left(\frac{\partial J^{\mathrm{NL}}}{\partial t}(t_n) + \frac{\partial J^{\mathrm{NL}}}{\partial t}(t_{n+1})\right)\frac{N_p(t_{n+1}) - N_p(t_n)}{\Delta t_{n+1}}\Big] \\ &\quad + \sum_{i=1}^{4}\left\{\mathcal{I}_{i\to\varphi}(\bar{\varphi})\Big[\frac{G_{p,i}(t_{n+1}) - G_{p,i}(t_n)}{E\big(\xi(t_{n+1})\big)\Delta t_{n+1}}\right. \\ &\quad \left. + \frac{\Delta t_{n+1}}{2}\left(\frac{\partial J^{\mathrm{NL}}}{\partial t}(t_n) + \frac{\partial J^{\mathrm{NL}}}{\partial t}(t_{n+1})\right)\frac{G_{p,i}(t_{n+1}) - G_{p,i}(t_n)}{\Delta t_{n+1}}\Big]\right\}\end{aligned} \tag{86}$$

$$
\begin{aligned}
&\frac{\theta_z^C(\xi,\bar{\varphi},t_{n+1})-\theta_z^C(\xi,\bar{\varphi},t_n)}{\Delta t_{n+1}}-\frac{\theta_{z,b}^C(t_{n+1})-\theta_{z,b}^C(t_n)}{\Delta t_{n+1}}\\
&=+\mathcal{I}_{N\to z}(\bar{\varphi})\left[\frac{N_p(t_{n+1})-N_p(t_n)}{E\big(\xi(t_{n+1})\big)\Delta t_{n+1}}\right.\\
&\quad\left.+\frac{\Delta t_{n+1}}{2}\left(\frac{\partial J^{\mathrm{NL}}}{\partial t}(t_n)+\frac{\partial J^{\mathrm{NL}}}{\partial t}(t_{n+1})\right)\frac{N_p(t_{n+1})-N_p(t_n)}{\Delta t_{n+1}}\right]\\
&\quad+\sum_{i=1}^{4}\left\{\mathcal{I}_{i\to z}(\bar{\varphi})\left[\frac{G_{p,i}(t_{n+1})-G_{p,i}(t_n)}{E\big(\xi(t_{n+1})\big)\Delta t_{n+1}}\right.\right.\\
&\quad\left.\left.+\frac{\Delta t_{n+1}}{2}\left(\frac{\partial J^{\mathrm{NL}}}{\partial t}(t_n)+\frac{\partial J^{\mathrm{NL}}}{\partial t}(t_{n+1})\right)\frac{G_{p,i}(t_{n+1})-G_{p,i}(t_n)}{\Delta t_{n+1}}\right]\right\}
\end{aligned}
\tag{87}
$$

whereby

$$
\frac{\partial J^{\mathrm{NL}}}{\partial t}(t_n)+\frac{\partial J^{\mathrm{NL}}}{\partial t}(t_{n+1})=\frac{\eta}{E_c\big(\xi(t_n)\big)}\frac{\beta}{t_0}\left[\frac{t_n}{t_0}\right]^{\beta-1}+\frac{\eta}{E_c\big(\xi(t_{n+1})\big)}\frac{\beta}{t_0}\left[\frac{t_{n+1}}{t_0}\right]^{\beta-1}. \tag{88}
$$

It is pointed out that for the affinity factor the level of loading is determined with the stresses of the pre-step. This requires the selection of sufficiently small time increments between the chosen time instants from Table 2.

4.3 Determination of the unknowns: ground pressure, axial force, and generator rotations at the ends of the circular segment

The preceding developments contain seven unknowns, four values for the ground pressure at different locations, one value for the axial force, and two values for the generator rotations at the beginning and at the end of the circular tunnel shell segment, respectively. In mathematical terms, these unknowns are: $G_{p,1}(t_i)$, $G_{p,2}(t_i)$, $G_{p,3}(t_i)$, $G_{p,4}(t_i)$, $N_p(t_i)$, $\theta_{z,b}^C(t_i)$, $\theta_{z,e}^C(t_i)$.
For the determination of these unknowns, seven equations are necessary. They are obtained as follows:

- Two equations result from the specification of the natural boundary condition (27) for the beginning of the arch segment $\bar{\varphi}=\varphi_b=0$ and for the end of the arch segment $\bar{\varphi}=\varphi_e=\Delta\varphi$, as well as for (33) and (34).
- Two equations result from the specification of the discretized format of the radial displacements according to (85) for $u_r^C(\xi,\bar{\varphi}=\Delta\varphi/2,t_i)=u_r^{\mathrm{MP1}}(t_i)$ and $u_r^C(\xi,\bar{\varphi}=\Delta\varphi,t_i)=u_r^{\mathrm{MP2}}(t_i)$.
- Two equations result from the specification of the discretized format of the tangential displacements (86) for $u_\varphi^C(\xi,\bar{\varphi}=\Delta\varphi/2,t_i)=u_\varphi^{\mathrm{MP1}}(t_i)$ and $u_\varphi^C(\xi,\bar{\varphi}=\Delta\varphi,t_i)=u_\varphi^{\mathrm{MP2}}(t_i)$.
- One equation results from the specification of the discretized format of the rotation angle (87) for $\theta_z^C(\xi,\bar{\varphi}=\Delta\varphi,t_i)=\theta_{z,c}^C(t_i)$.

For the geometrical and material properties from Sect. 4.1 and the displacement measurements given in Table 2, the solution of the aforementioned linear system of equations for twenty time points t_i yields the following results: (i) the ground pressure values $G_{p,1}$, $G_{p,2}$, $G_{p,3}$, and $G_{p,4}$ are almost identical, expressing a uniform ground pressure distribution along the circumference of the tunnel segment, see Fig. 7; (ii) compressive axial forces N_p are acting on the imposts, and the use of corresponding values in (32) yields axial forces which are again uniform along the circumferential direction of the tunnel segment, see Fig. 8a–d; (iii) the generator rotations, $\theta_{z,b}^C$ and $\theta_{z,e}^C$, differ largely from one another, and the use of $\theta_{z,b}^C$ and of the aforementioned force and pressure values in (68) and (69) yields a non-uniform distribution of generator rotations along the tunnel segment circumference, see Fig. 9i–l.

The results are further complemented by the use of the force and pressure values, N_p and $G_{p,i}$, with $i=1,2,3,4$, in (33), yielding the non-uniform bending moment distribution seen in Fig. 10; these moments are, however, very small, as can be seen from excentricities amounting to $m_\varphi/n_\varphi\approx 0.001$ m. Moreover, use of the aforementioned force and pressure values, together with the measured displacements u_r^{MP3} and u_φ^{MP3} and the computed generation rotations $\theta_{z,b}^C$, in (62)–(67), yields the displacement distributions of Fig. 9 (a–h). Use of the latter displacement distribution in expression (51) for the circumferential normal strain, inserting

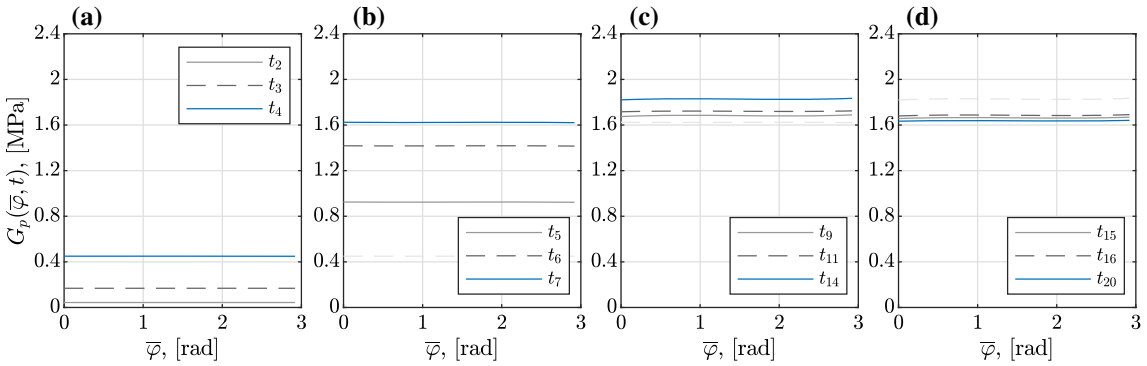

Fig. 7 Distribution of ground pressure along the circumference of the top heading of the Sieberg tunnel at measurement cross section MC 1452, for different time points according to Table 2

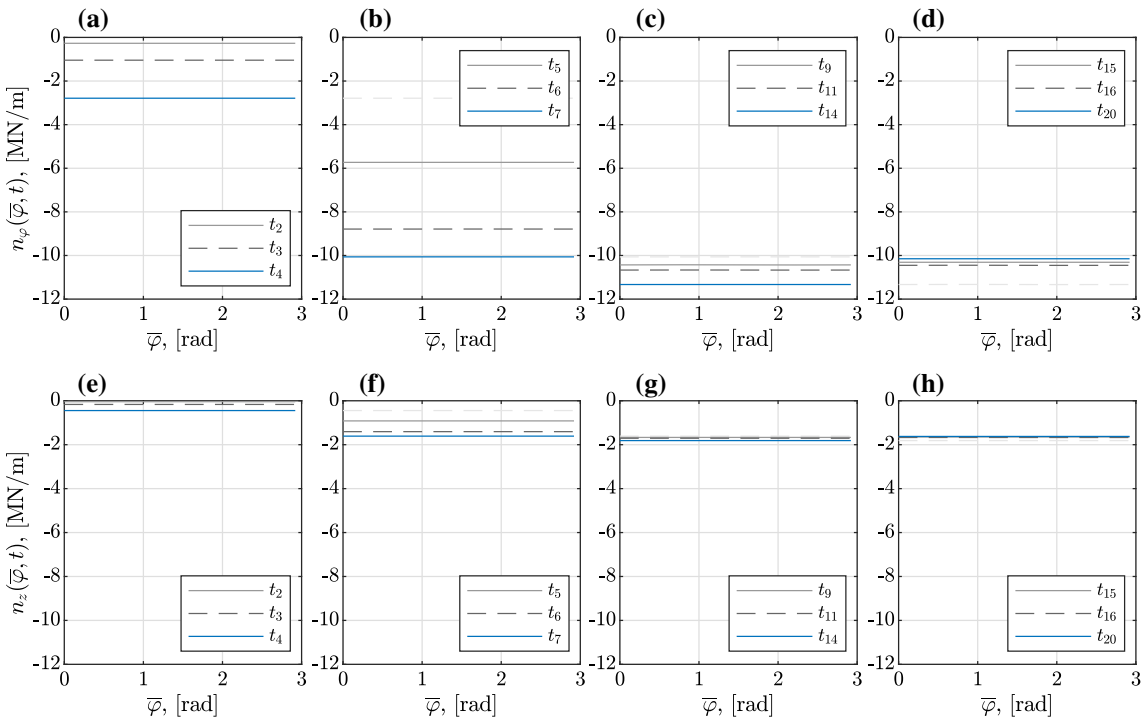

Fig. 8 Distribution of **a**–**d** circumferential and **e**–**h** axial normal forces along the circumference of the top heading of the Sieberg tunnel at measurement cross section MC 1452, for different time points according to Table 2

the result into (48.2) while considering (49.2), and defining the axial normal force by replacing, in (17), "φ" by "z", yields

$$n_z(\bar{\varphi}, t) = \nu(1-\nu)\, n_\varphi(\bar{\varphi}, t), \tag{89}$$

see Fig. 8e–h for corresponding results. From an evolutionary perspective, the normal forces and ground pressures heavily increase during the first days in the life time of the tunnel segment installed at MC1452 of the Sieberg tunnel, and stay nearly constant thereafter, see Fig. 11. Finally, the degree of utilization is computed from insertion of the displacement values of Fig. 9a–h into Eq. (51), and of the corresponding result into (48.1) while considering (48.2), see Fig. 12. As with the force and pressure evolutions, the degree of utilization exhibits a strong increase during the first days of the life of the tunnel shell, followed by a mild decrease.

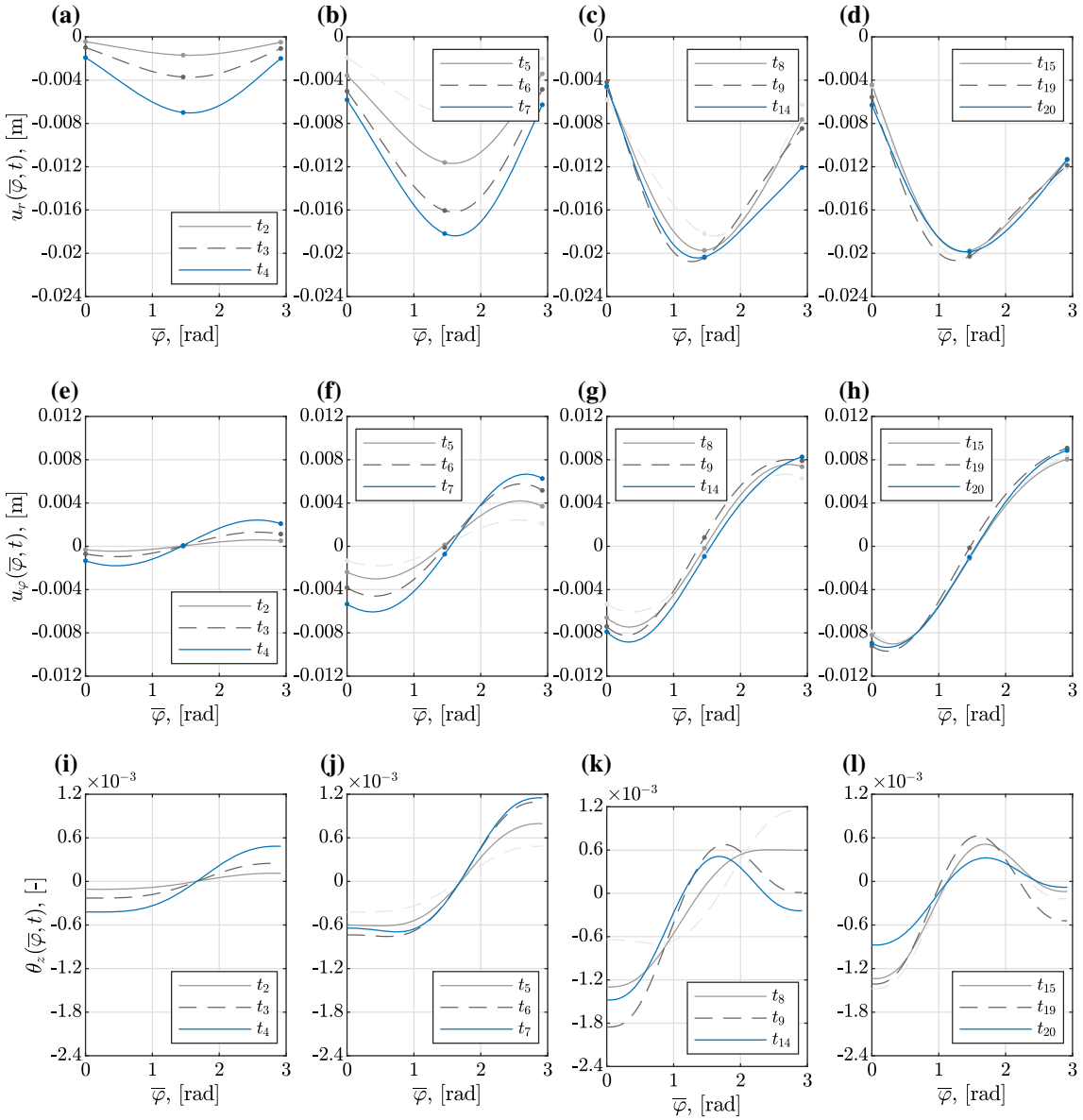

Fig. 9 Distribution of radial **a–d** and circumferential **e–h** displacements, and of **i–l** generator rotations along the circumference of the top heading of the Sieberg tunnel at measurement cross section MC 1452, for different time points according to Table 2

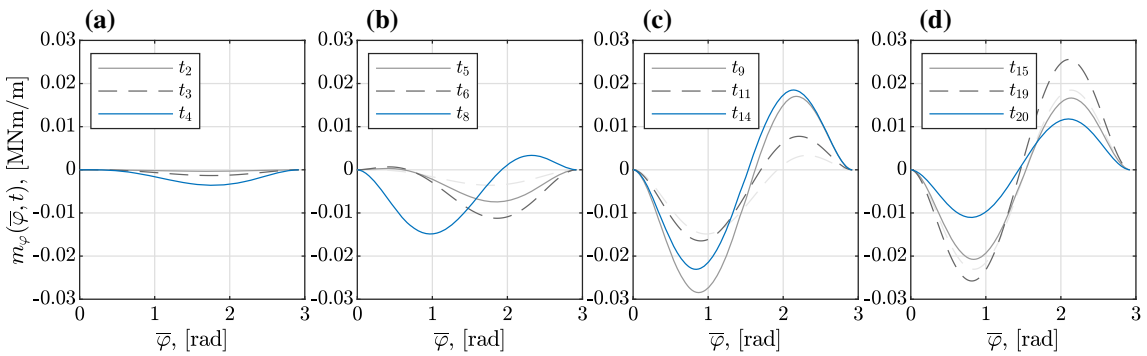

Fig. 10 Distribution of bending moments along the circumference of the top heading of the Sieberg tunnel at measurement cross section MC 1452, for different time points according to Table 2

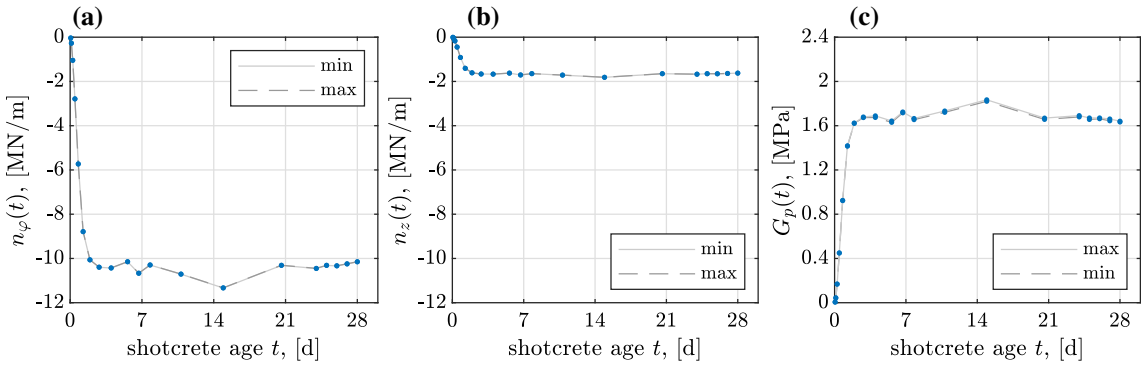

Fig. 11 Evolution over time of **a** circumferential and **b** axial normal force as well as **c** ground pressure of the top heading of the Sieberg tunnel at measurement cross section MC 1452

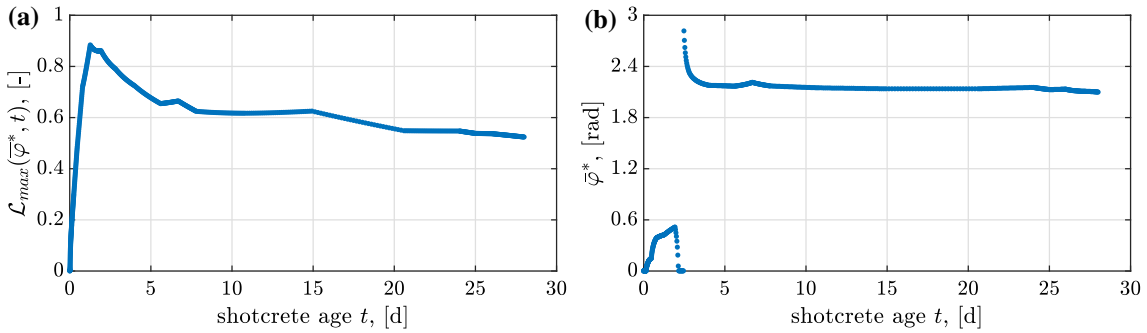

Fig. 12 History of degree of utilization (**a**) and its position (**b**) of the top heading of the Sieberg tunnel at measurement cross section MC 1452

5 Conclusions

The consideration of polar components of point-wise measured displacement vectors in combination with a tunnel-specific shell theory and the viscoelastic modeling of aging shotcrete provides analytical access to the ground pressure distribution along the tunnel circumference, impost forces, and all quantities arising from the action of the latter external forces: distributions of all internal normal forces and bending moments, of radial and circumferential displacements, and of the degree of utilization.

The "white-box" nature of this approach, providing a closed-form expression for advanced mechanics-driven data evaluation, renders it, in the opinion of the authors, as a prime source for reliable and clear rule development in the ongoing discussion concerning artificial intelligence and "big data" in geotechnical engineering. In particular, the presented concept can be straightforwardly extended towards more complex geometries and construction sequences. This task is planned in close interaction with the tunnel engineering industry.

At the same time, and from a more pragmatic perspective, our approach also provides novel insights which may support the calibration of state-of-the-art Finite Element models encompassing the tunnel shell and the bolt-reinforced rock [21].

Funding Open access funding provided by TU Wien Bibliothek.

Acknowledgements The authors gratefully acknowledge project FFG-COMET #882504 "Rail4Future: Resilient Digital Railway Systems to enhance performance".

A Approximation of the concrete strength—based on a micro-to-macro validated engineering mechanics model

[18] provides a mathematical approximation for the uniaxial compressive strength of concrete, as a function of material composition and maturity, i.e., a combination of the effective water-to-cement mass ratios $(w/c)_{eff}$, the aggregate-to-cement mass ratio a/c, the volume fractions of aggregates $f_{\text{agg}}^{\text{con}}$ and the hydration degree ξ. In more detail the uniaxial compressive strength of the hydrate phase results from the Mohr-Coulomb failure criterion as

$$\Sigma_{\text{hyd}}^{\text{uni, ult}} = \frac{2c_{\text{hyd}}\cos(\varphi_{\text{hyd}})}{1-\sin(\varphi_{\text{hyd}})} = 123.49\,\text{MPa} \tag{90}$$

with cohesion $c_{\text{hyd}} = 50\,\text{MPa}$ and friction angle $\varphi_{\text{hyd}} = 12°$. The uniaxial compressive strength of the hydrate foam can be expressed as

$$\begin{aligned}\Sigma_{hf}^{\text{uni, ult}} = \Sigma_{\text{hyd}}^{\text{uni, ult}}\Big\{&-2.853\,(f_{\text{hyd}}^{\text{hf}})^5 + 5.764\,(f_{\text{hyd}}^{\text{hf}})^4 - 2.746\,(f_{\text{hyd}}^{\text{hf}})^3\\ &+0.7084\,(f_{\text{hyd}}^{\text{hf}})^2 + 0.08728\,(f_{\text{hyd}}^{\text{hf}})\Big\}\end{aligned} \tag{91}$$

with the hydrate foam-related corresponding volume fraction $f_{\text{hyd}}^{\text{hf}}$ as function of the (effective) w/c-ratio and hydration degree ξ,

$$f_{\text{hyd}}^{\text{hf}} = \frac{43.15\xi}{20\xi + 63(w/c)_{eff}}. \tag{92}$$

The uniaxial compressive strength of the cement paste can be expressed as

$$\Sigma_{cp}^{\text{uni, ult}} = \Sigma_{hf}^{\text{uni, ult}}\Big\{1 + C_1 f_{\text{clin}}^{\text{cp}} + C_2 f_{\text{clin}}^{\text{cp}}\Big\} \tag{93}$$

with the cement paste-related clinker volume fraction $f_{\text{clin}}^{\text{cp}}$

$$f_{\text{clin}}^{\text{cp}} = \frac{20(1-\xi)}{20 + 63(w/c)_{eff}} \tag{94}$$

and the constants C_1 and C_2,

$$\begin{aligned}C_1 &= +1.2789\,(f_{\text{hyd}}^{\text{hf}})^4 - 2.4825\,(f_{\text{hyd}}^{\text{hf}})^3 + 1.1613\,(f_{\text{hyd}}^{\text{hf}})^2 - 0.2398\,(f_{\text{hyd}}^{\text{hf}}) + 0.7317,\\ C_2 &= -0.3409\,(f_{\text{hyd}}^{\text{hf}})^4 + 0.7091\,(f_{\text{hyd}}^{\text{hf}})^3 - 0.3908\,(f_{\text{hyd}}^{\text{hf}})^2 + 0.0639\,(f_{\text{hyd}}^{\text{hf}}) - 0.1072.\end{aligned} \tag{95}$$

Finally, the uniaxial compressive strength of the concrete yields

$$\Sigma_{con}^{\text{uni, ult}} = \Sigma_{cp}^{\text{uni, ult}}\Big\{C_4\Big[1 + C_3(f_{\text{agg}}^{\text{con}} - 0.7)\Big]\Big\} \tag{96}$$

with the aggregate volume fraction as function of the (initial) aggregate-to-cement ratio (a/c), (initial) water-to-cement ratio (w/c), and the mass densities of aggregates, clinker and water, ρ_{agg}, ρ_{clin}, and $\rho_{\text{H}_2\text{O}}$

$$f_{\text{agg}}^{\text{con}} = \frac{\frac{a/c}{\rho_{\text{agg}}}}{\frac{1}{\rho_{\text{clin}}} + \frac{w/c}{\rho_{\text{H}_2\text{O}}} + \frac{a/c}{\rho_{\text{agg}}}}, \tag{97}$$

and the constants C_3 and C_4 are

$$\begin{aligned}C_3 &= +10.936\,(f_{\text{hyd}}^{\text{hf}})^4 - 35.766\,(f_{\text{hyd}}^{\text{hf}})^3 + 41.348\,(f_{\text{hyd}}^{\text{hf}})^2 - 20.096\,(f_{\text{hyd}}^{\text{hf}}) + 3.9162,\\ C_4 &= +2.8254\,(f_{\text{hyd}}^{\text{hf}})^4 - 7.5492\,(f_{\text{hyd}}^{\text{hf}})^3 + 7.1044\,(f_{\text{hyd}}^{\text{hf}})^2 - 2.8232\,(f_{\text{hyd}}^{\text{hf}}) + 1.3040.\end{aligned} \tag{98}$$

For a known shotcrete composition, the development over time of the uniaxial compressive strength of concrete can be described by (96), and simultaneously by means of the *fib* Model Code according to (35). Equating these two relations, while choosing specific model code quantities (namely, uniaxial compressive strength values reached after 28 days, which amount to of 50, 55, and 60 MPa; and a strength evolution parameter of $s_E = 0.18$) and compositional characteristics ((effective) water-to-cement ratios $(w/c)_{eff} \in \{0.450, 0.475, 0.500, 0.525\}$ and $f_{\text{agg}}^{\text{con}} = 0.70$ based on the concrete composition for the test campaign ULB I according to [18]), one arrives at evolutions of the degree of hydration as shown in Figs. 4 and 5.

B Time-invariant influence functions

The time-invariant influence functions $\mathcal{I}$ for the radial displacements can be expressed as

$$\begin{aligned}\mathcal{I}_{N\to r}(\bar{\varphi}) = \left\{1-\nu^2\right\}\Bigg\{\frac{12R^3}{h^3}\Big[\cos(\bar{\varphi})-1\Big]+\Big[\frac{R}{2h}+\frac{6R^3}{h^3}\Big]\Big[\frac{\bar{\varphi}\cos(\bar{\varphi})}{\tan(\Delta\varphi)} \\ +\bar{\varphi}\sin(\bar{\varphi})-\frac{\sin(\bar{\varphi})}{\tan(\Delta\varphi)}+\frac{\sin(\bar{\varphi})}{\sin(\Delta\varphi)}-\frac{\bar{\varphi}\cos(\bar{\varphi})}{\sin(\Delta\varphi)}\Big]\Bigg\},\end{aligned} \tag{99}$$

$$\begin{aligned}\mathcal{I}_{1\to r}(\bar{\varphi}) = \left\{1-\nu^2\right\}\Bigg\{\Big[\frac{R^2}{h}+\frac{12R^4}{h^3}\Big]\Big[-1-\frac{54\bar{\varphi}}{(\Delta\varphi)^3}+\frac{9\bar{\varphi}^3}{2(\Delta\varphi)^3}+\frac{36}{(\Delta\varphi)^2} \\ -\frac{9\bar{\varphi}^2}{(\Delta\varphi)^2}+\frac{11\bar{\varphi}}{2\Delta\varphi}-\frac{36\cos(\bar{\varphi})}{(\Delta\varphi)^2}+\frac{\bar{\varphi}\cos(\bar{\varphi})}{2\tan(\Delta\varphi)}-\frac{9\bar{\varphi}\cos(\bar{\varphi})}{(\Delta\varphi)^2\tan(\Delta\varphi)} \\ +\cos(\bar{\varphi})-\frac{9\bar{\varphi}\cos(\bar{\varphi})}{2(\Delta\varphi)^2\sin(\Delta\varphi)}+\frac{\bar{\varphi}\sin(\bar{\varphi})}{2}+\frac{54\sin(\bar{\varphi})}{(\Delta\varphi)^3}-\frac{9\bar{\varphi}\sin(\bar{\varphi})}{(\Delta\varphi)^2} \\ -\frac{11\sin(\bar{\varphi})}{2\Delta\varphi}-\frac{\sin(\bar{\varphi})}{2\tan(\Delta\varphi)}+\frac{9\sin(\bar{\varphi})}{(\Delta\varphi)^2\tan(\Delta\varphi)}+\frac{9\sin(\bar{\varphi})}{2(\Delta\varphi)^2\sin(\Delta\varphi)}\Big]\Bigg\},\end{aligned} \tag{100}$$

$$\begin{aligned}\mathcal{I}_{2\to r}(\bar{\varphi}) = \left\{1-\nu^2\right\}\Bigg\{\Big[\frac{R^2}{h}+\frac{12R^4}{h^3}\Big]\Big[\frac{162\bar{\varphi}}{(\Delta\varphi)^3}-\frac{27\bar{\varphi}^3}{2(\Delta\varphi)^3}-\frac{90}{(\Delta\varphi)^2}+\frac{45\bar{\varphi}^2}{2(\Delta\varphi)^2} \\ -\frac{9\bar{\varphi}}{\Delta\varphi}+\frac{90\cos(\bar{\varphi})}{(\Delta\varphi)^2}+\frac{45\bar{\varphi}\cos(\bar{\varphi})}{2(\Delta\varphi)^2\tan(\Delta\varphi)} \\ +\frac{18\bar{\varphi}\cos(\bar{\varphi})}{(\Delta\varphi)^2\sin(\Delta\varphi)}-\frac{162\sin(\bar{\varphi})}{(\Delta\varphi)^3}+\frac{45\bar{\varphi}\sin(\bar{\varphi})}{2(\Delta\varphi)^2} \\ +\frac{9\sin(\bar{\varphi})}{\Delta\varphi}-\frac{45\sin(\bar{\varphi})}{2(\Delta\varphi)^2\tan(\Delta\varphi)}-\frac{18\sin(\bar{\varphi})}{(\Delta\varphi)^2\sin(\Delta\varphi)}\Big]\Bigg\},\end{aligned} \tag{101}$$

$$\begin{aligned}\mathcal{I}_{3\to r}(\bar{\varphi}) = \left\{1-\nu^2\right\}\Bigg\{\Big[\frac{R^2}{h}+\frac{12R^4}{h^3}\Big]\Big[-\frac{162\bar{\varphi}}{(\Delta\varphi)^3}+\frac{27\bar{\varphi}^3}{2(\Delta\varphi)^3}+\frac{72}{(\Delta\varphi)^2}-\frac{18\bar{\varphi}^2}{(\Delta\varphi)^2} \\ +\frac{9\bar{\varphi}}{2\Delta\varphi}-\frac{72\cos(\bar{\varphi})}{(\Delta\varphi)^2}-\frac{18\bar{\varphi}\cos(\bar{\varphi})}{(\Delta\varphi)^2\tan(\Delta\varphi)} \\ -\frac{45\bar{\varphi}\cos(\bar{\varphi})}{2(\Delta\varphi)^2\sin(\Delta\varphi)}+\frac{162\sin(\bar{\varphi})}{(\Delta\varphi)^3}-\frac{18\bar{\varphi}\sin(\bar{\varphi})}{(\Delta\varphi)^2} \\ -\frac{9\sin(\bar{\varphi})}{2\Delta\varphi}+\frac{18\sin(\bar{\varphi})}{(\Delta\varphi)^2\tan(\Delta\varphi)}+\frac{45\sin(\bar{\varphi})}{2(\Delta\varphi)^2\sin(\Delta\varphi)}\Big]\Bigg\},\end{aligned} \tag{102}$$

$$\begin{aligned}\mathcal{I}_{4\to r}(\bar{\varphi}) = \left\{1-\nu^2\right\}\Bigg\{\Big[\frac{R^2}{h}+\frac{12R^4}{h^3}\Big]\Big[\frac{54\bar{\varphi}}{(\Delta\varphi)^3}-\frac{9\bar{\varphi}^3}{2(\Delta\varphi)^3}-\frac{18}{(\Delta\varphi)^2}+\frac{9\bar{\varphi}^2}{2(\Delta\varphi)^2} \\ -\frac{\bar{\varphi}}{\Delta\varphi}+\frac{18\cos(\bar{\varphi})}{(\Delta\varphi)^2}+\frac{9\bar{\varphi}\cos(\bar{\varphi})}{2(\Delta\varphi)^2\tan(\Delta\varphi)}-\frac{54\sin(\bar{\varphi})}{(\Delta\varphi)^3} \\ +\frac{9\bar{\varphi}\cos(\bar{\varphi})}{(\Delta\varphi)^2\sin(\Delta\varphi)}+\frac{9\bar{\varphi}\sin(\bar{\varphi})}{2(\Delta\varphi)^2}-\frac{\bar{\varphi}\cos(\bar{\varphi})}{2\sin(\Delta\varphi)}+\frac{\sin(\bar{\varphi})}{\Delta\varphi} \\ -\frac{9\sin(\bar{\varphi})}{2(\Delta\varphi)^2\tan(\Delta\varphi)}+\frac{\sin(\bar{\varphi})}{2\sin(\Delta\varphi)}-\frac{9\sin(\bar{\varphi})}{(\Delta\varphi)^2\sin(\Delta\varphi)}\Big]\Bigg\}.\end{aligned} \tag{103}$$

The time-invariant influence functions $\mathcal{I}$ for the tangential displacements can be expressed as

$$\begin{aligned}\mathcal{I}_{N\to\varphi}(\bar{\varphi}) = &\left\{1-\nu^2\right\}\left\{\left[\frac{R}{2h}+\frac{6R^3}{h^3}\right]\left[+\bar{\varphi}\cos(\bar{\varphi})-3\sin(\bar{\varphi})-\frac{\bar{\varphi}\sin(\bar{\varphi})}{\tan(\Delta\varphi)}+\frac{\bar{\varphi}\sin(\bar{\varphi})}{\sin(\Delta\varphi)}\right]\right.\\ &\left.+\frac{R}{h}\left[+2\sin(\bar{\varphi})\right]+\frac{12R^3}{h^3}\left[+\bar{\varphi}-\frac{\cos(\bar{\varphi})-1}{\tan(\Delta\varphi)}+\frac{\cos(\bar{\varphi})-1}{\sin(\Delta\varphi)}\right]\right\},\end{aligned} \tag{104}$$

$$\begin{aligned}\mathcal{I}_{1\to\varphi}(\bar{\varphi}) = &\left\{1-\nu^2\right\}\left\{\left[\frac{R^2}{h}+\frac{12R^4}{h^3}\right]\left[-\frac{54-54\cos(\bar{\varphi})}{(\Delta\varphi)^3}+\frac{11-11\cos(\bar{\varphi})}{2\Delta\varphi}\right.\right.\\ &+\frac{\bar{\varphi}\cos(\bar{\varphi})}{2}-\frac{9\bar{\varphi}\cos(\bar{\varphi})}{(\Delta\varphi)^2}-\frac{\bar{\varphi}\sin(\bar{\varphi})}{2\tan(\Delta\varphi)}+\frac{9\bar{\varphi}\sin(\bar{\varphi})}{(\Delta\varphi)^2\tan(\Delta\varphi)}\\ &\left.+\frac{9\bar{\varphi}\sin(\bar{\varphi})}{2(\Delta\varphi)^2\sin(\Delta\varphi)}\right]+\frac{R^2}{h}\left[+\frac{27\bar{\varphi}^2}{2(\Delta\varphi)^3}-\frac{18\bar{\varphi}}{(\Delta\varphi)^2}-\frac{\sin(\bar{\varphi})}{2}\right.\\ &+\frac{27\sin(\bar{\varphi})}{(\Delta\varphi)^2}\Big]+\frac{12R^4}{h^3}\left[\frac{3\bar{\varphi}^3}{(\Delta\varphi)^2}-\frac{9\bar{\varphi}^4}{8(\Delta\varphi)^3}-\frac{11\bar{\varphi}^2}{4\Delta\varphi}\right.\\ &+\frac{27\bar{\varphi}^2}{(\Delta\varphi)^3}-\frac{36\bar{\varphi}}{(\Delta\varphi)^2}-\frac{3\sin(\bar{\varphi})}{2}+\frac{45\sin(\bar{\varphi})}{(\Delta\varphi)^2}\\ &\left.\left.-\frac{9-9\cos(\bar{\varphi})}{(\Delta\varphi)^2\sin(\Delta\varphi)}+\frac{1-\cos(\bar{\varphi})}{\tan(\Delta\varphi)}-\frac{18-18\cos(\bar{\varphi})}{(\Delta\varphi)^2\tan(\Delta\varphi)}+\bar{\varphi}\right]\right\},\end{aligned} \tag{105}$$

$$\begin{aligned}\mathcal{I}_{2\to\varphi}(\bar{\varphi}) = &\left\{1-\nu^2\right\}\left\{\left[\frac{R^2}{h}+\frac{12R^4}{h^3}\right]\left[+\frac{162-162\cos(\bar{\varphi})}{(\Delta\varphi)^3}-\frac{9-9\cos(\bar{\varphi})}{\Delta\varphi}\right.\right.\\ &\left.-\frac{45\bar{\varphi}\sin(\bar{\varphi})}{2(\Delta\varphi)^2\tan(\Delta\varphi)}-\frac{18\bar{\varphi}\sin(\bar{\varphi})}{(\Delta\varphi)^2\sin(\Delta\varphi)}+\frac{45\bar{\varphi}\cos(\bar{\varphi})}{2(\Delta\varphi)^2}\right]\\ &+\frac{12R^4}{h^3}\left[-\frac{81\bar{\varphi}^2}{(\Delta\varphi)^3}+\frac{27\bar{\varphi}^4}{8(\Delta\varphi)^3}+\frac{90\bar{\varphi}}{(\Delta\varphi)^2}-\frac{15\bar{\varphi}^3}{2(\Delta\varphi)^2}\right.\\ &+\frac{9\bar{\varphi}^2}{2\Delta\varphi}+\frac{45-45\cos(\bar{\varphi})}{(\Delta\varphi)^2\tan(\Delta\varphi)}+\frac{36-36\cos(\bar{\varphi})}{(\Delta\varphi)^2\sin(\Delta\varphi)}\\ &\left.-\frac{225\sin(\bar{\varphi})}{2(\Delta\varphi)^2}\right]+\frac{R^2}{h}\left[-\frac{81\bar{\varphi}^2}{2(\Delta\varphi)^3}+\frac{45\bar{\varphi}}{(\Delta\varphi)^2}-\frac{135\sin(\bar{\varphi})}{2(\Delta\varphi)^2}\right]\Big\},\end{aligned} \tag{106}$$

$$\begin{aligned}\mathcal{I}_{3\to\varphi}(\bar{\varphi}) = &\left\{1-\nu^2\right\}\left\{\left[\frac{R^2}{h}+\frac{12R^4}{h^3}\right]\left[-\frac{162-162\cos(\bar{\varphi})}{(\Delta\varphi)^3}+\frac{9-9\cos(\bar{\varphi})}{2\Delta\varphi}\right.\right.\\ &\left.-\frac{18\bar{\varphi}\cos(\bar{\varphi})}{(\Delta\varphi)^2}+\frac{18\bar{\varphi}\sin(\bar{\varphi})}{(\Delta\varphi)^2\tan(\Delta\varphi)}+\frac{45\bar{\varphi}\sin(\bar{\varphi})}{2(\Delta\varphi)^2\sin(\Delta\varphi)}\right]\\ &+\frac{12R^4}{h^3}\left[\frac{81\bar{\varphi}^2}{(\Delta\varphi)^3}-\frac{27\bar{\varphi}^4}{8(\Delta\varphi)^3}-\frac{72\bar{\varphi}}{(\Delta\varphi)^2}+\frac{6\bar{\varphi}^3}{(\Delta\varphi)^2}\right.\\ &-\frac{9\bar{\varphi}^2}{4\Delta\varphi}-\frac{36-36\cos(\bar{\varphi})}{(\Delta\varphi)^2\tan(\Delta\varphi)}-\frac{45-45\cos(\bar{\varphi})}{(\Delta\varphi)^2\sin(\Delta\varphi)}\\ &\left.+\frac{90\sin(\bar{\varphi})}{(\Delta\varphi)^2}\right]+\frac{R^2}{h}\left[\frac{81\bar{\varphi}^2}{2(\Delta\varphi)^3}-\frac{36\bar{\varphi}}{(\Delta\varphi)^2}+\frac{54\sin(\bar{\varphi})}{(\Delta\varphi)^2}\right]\Big\},\end{aligned} \tag{107}$$

$$\begin{aligned}\mathcal{I}_{4\to\varphi}(\bar{\varphi}) = &\left\{1-\nu^2\right\}\left\{\left[\frac{R^2}{h}+\frac{12R^4}{h^3}\right]\left[-\frac{1}{\Delta\varphi}+\frac{54-54\cos(\bar{\varphi})}{\Delta\varphi^3}+\frac{9\bar{\varphi}\cos(\bar{\varphi})}{2\Delta\varphi^2}\right.\right.\\ &-\frac{9\bar{\varphi}\sin(\bar{\varphi})}{2\Delta\varphi^2\tan(\Delta\varphi)}+\frac{\bar{\varphi}\sin(\bar{\varphi})}{2\sin(\Delta\varphi)}-\frac{9\bar{\varphi}\sin(\bar{\varphi})}{\Delta\varphi^2\sin(\Delta\varphi)}\\ &\left.+\frac{\cos(\bar{\varphi})}{\Delta\varphi}\right]+\frac{12R^4}{h^3}\left[-\frac{27\bar{\varphi}^2}{\Delta\varphi^3}+\frac{9\bar{\varphi}^4}{8\Delta\varphi^3}+\frac{18\bar{\varphi}}{\Delta\varphi^2}-\frac{3\bar{\varphi}^3}{2\Delta\varphi^2}\right.\\ &+\frac{\bar{\varphi}^2}{2\Delta\varphi}-\frac{45\sin(\bar{\varphi})}{2\Delta\varphi^2}+\frac{9-9\cos(\bar{\varphi})}{\Delta\varphi^2\tan(\Delta\varphi)}-\frac{1-\cos(\bar{\varphi})}{\sin(\Delta\varphi)}\\ &\left.+\frac{18-18\cos(\bar{\varphi})}{\Delta\varphi^2\sin(\Delta\varphi)}\right]+\frac{R^2}{h}\left[+\frac{9\bar{\varphi}}{\Delta\varphi^2}-\frac{27\bar{\varphi}^2}{2\Delta\varphi^3}-\frac{27\sin(\bar{\varphi})}{2\Delta\varphi^2}\right]\Big\}.\end{aligned} \tag{108}$$

The time-invariant influence functions $\mathcal{I}$ for the cross-sectional rotation angle can be expressed as

$$\mathcal{I}_{N\to z}(\bar{\varphi}) = \left\{1-\nu^2\right\}\left\{\frac{12R^2}{h^3}\left[\frac{\cos(\bar{\varphi})-1}{\tan(\Delta\varphi)}+\frac{1-\cos(\bar{\varphi})}{\sin(\Delta\varphi)}+\sin(\bar{\varphi})-\bar{\varphi}\right]\right\}, \tag{109}$$

$$\begin{aligned}\mathcal{I}_{1\to z}(\bar{\varphi}) = \left\{1-\nu^2\right\}\Bigg\{\frac{12R^3}{h^3}\Bigg[&-\bar{\varphi}-\frac{27\bar{\varphi}^2}{2(\Delta\varphi)^3}+\frac{9\bar{\varphi}^4}{8(\Delta\varphi)^3}+\frac{18\bar{\varphi}}{(\Delta\varphi)^2}-\frac{3\bar{\varphi}^3}{(\Delta\varphi)^2}\\&+\frac{11\bar{\varphi}^2}{4\Delta\varphi}-\frac{1-\cos(\bar{\varphi})}{\tan(\Delta\varphi)}+\sin(\bar{\varphi})\\&-\frac{18\sin(\bar{\varphi})}{(\Delta\varphi)^2}+\frac{18-18\cos(\bar{\varphi})}{(\Delta\varphi)^2\tan(\Delta\varphi)}+\frac{9-9\cos(\bar{\varphi})}{(\Delta\varphi)^2\sin(\Delta\varphi)}\Bigg]\Bigg\},\end{aligned} \tag{110}$$

$$\begin{aligned}\mathcal{I}_{2\to z}(\bar{\varphi}) = \left\{1-\nu^2\right\}\Bigg\{\frac{12R^3}{h^3}\Bigg[&+\frac{81\bar{\varphi}^2}{2(\Delta\varphi)^3}-\frac{27\bar{\varphi}^4}{8(\Delta\varphi)^3}-\frac{45\bar{\varphi}}{(\Delta\varphi)^2}+\frac{15\bar{\varphi}^3}{2(\Delta\varphi)^2}\\&-\frac{9\bar{\varphi}^2}{2\Delta\varphi}+\frac{45\sin(\bar{\varphi})}{(\Delta\varphi)^2}-\frac{45-45\cos(\bar{\varphi})}{(\Delta\varphi)^2\tan(\Delta\varphi)}-\frac{36-36\cos(\bar{\varphi})}{(\Delta\varphi)^2\sin(\Delta\varphi)}\Bigg]\Bigg\},\end{aligned} \tag{111}$$

$$\begin{aligned}\mathcal{I}_{3\to z}(\bar{\varphi}) = \left\{1-\nu^2\right\}\Bigg\{\frac{12R^3}{h^3}\Bigg[&-\frac{81\bar{\varphi}^2}{2(\Delta\varphi)^3}+\frac{27\bar{\varphi}^4}{8(\Delta\varphi)^3}+\frac{36\bar{\varphi}}{(\Delta\varphi)^2}-\frac{6\bar{\varphi}^3}{(\Delta\varphi)^2}\\&+\frac{9\bar{\varphi}^2}{4\Delta\varphi}-\frac{36\sin(\bar{\varphi})}{(\Delta\varphi)^2}+\frac{36-36\cos(\bar{\varphi})}{(\Delta\varphi)^2\tan(\Delta\varphi)}+\frac{45-45\cos(\bar{\varphi})}{(\Delta\varphi)^2\sin(\Delta\varphi)}\Bigg]\Bigg\},\end{aligned} \tag{112}$$

$$\begin{aligned}\mathcal{I}_{4\to z}(\bar{\varphi}) = \left\{1-\nu^2\right\}\Bigg\{\frac{12R^3}{h^3}\Bigg[&+\frac{27\bar{\varphi}^2}{2(\Delta\varphi)^3}-\frac{9\bar{\varphi}^4}{8(\Delta\varphi)^3}-\frac{9\bar{\varphi}}{(\Delta\varphi)^2}+\frac{3\bar{\varphi}^3}{2(\Delta\varphi)^2}-\frac{\bar{\varphi}^2}{2\Delta\varphi}\\&+\frac{9\sin(\bar{\varphi})}{(\Delta\varphi)^2}-\frac{9-9\cos(\bar{\varphi})}{(\Delta\varphi)^2\tan(\Delta\varphi)}-\frac{18-18\cos(\bar{\varphi})}{(\Delta\varphi)^2\sin(\Delta\varphi)}+\frac{1-\cos(\bar{\varphi})}{\sin(\Delta\varphi)}\Bigg]\Bigg\}.\end{aligned} \tag{113}$$

References

1. Ausweger, M., Binder, E., Lahayne, O., Reihsner, R., Maier, G., Peyerl, M., Pichler, B.: Early-age evolution of strength, stiffness, and non-aging creep of concretes: experimental characterization and correlation analysis. Materials **12**(2), 481–489 (2019). https://doi.org/10.3390/ma12020207
2. Brandtner, M., Moritz, B., Schubert, P.: On the challenge of evaluating stress in a shotcrete lining: experiences gained in applying the hybrid analysis method. Felsbau **25**(5), 93–98 (2007)
3. Carranza-Torres, C., Fairhurst, C.: Application of the convergence-confinement method of tunnel design to rock masses that satisfy the Hoek-Brown failure criterion. Tunnell. Underground Space Technol. **15**(2), 187–213 (2000). https://doi.org/10.1016/S0886-7798(00)00046-8
4. CEB-FIB: Model Code for Concrete Structures 2010. Ernst & Sohn, Berlin, Germany (2010)
5. Fenner, R.: Untersuchungen zur Erkenntnis des Gebirgsdrucks [Investigations to the knowledge of the rock pressure]. Glückauf, Berg- und Hüttenmännische Zeitschrift **32**, 681–695 (1938)
6. Fosdick, R.: Observations concerning virtual power. Math. Mech. Solids **16**(6), 573–585 (2011). https://doi.org/10.1177/1081286510387708
7. Germain, P.: Méchanique des milieux continus. C. R. Acad. Sc. Paris **Série A**(t.274), 1051–1055 (1972)
8. Germain, P.: La méthode des puissances virtuelles en mécanique des milieux continus. I: Théorie du second gradient. J. de Mécanique **12**(2), 235–274 (1973)
9. Germain, P.: The method of virtual power in continuum mechanics. part 2: microstructure. SIAM J. Appl. Math. **25**(3), 556–575 (1973). https://doi.org/10.1137/0125053
10. Germain, P.: The method of virtual power in the mechanics of continuous media. I: second-gradient theory. Math. Mech. Complex Syst. **8**(2), 153–190 (2020). https://doi.org/10.2140/memocs.2020.8.153
11. Hellmich, C., Macht, J., Mang, H.: Ein hybrides Verfahren zur Bestimmung der Auslastung von Spritzbetonschalen [A hybrid method for determination of the degree of utilization of shotcrete tunnel shells]. Felsbau **17**(5), 422–425 (1999)
12. Hellmich, C., Mang, H., Ulm, F.: Hybrid method for quantification of stress states in shotcrete tunnel shells: combination of 3D in situ displacement measurements and thermochemoplastic material law. Comput. Struct. **79**(22–25), 2103–2115 (2001). https://doi.org/10.1016/S0045-7949(01)00057-8
13. Höller, R., Aminbaghai, M., Eberhardsteiner, L., Eberhardsteiner, J., Blab, R., Pichler, B., Hellmich, C.: Rigorous amendment of Vlasov's theory for thin elastic plates on elastic Winkler foundations, based on the Principle of Virtual Power. Eur. J. Mech. A. Solids **73**, 449–482 (2019). https://doi.org/10.1016/j.euromechsol.2018.07.013
14. Irfan-ul Hassan, M., Pichler, B., Reihsner, R., Hellmich, C.: Elastic and creep properties of young cement paste, as determined from hourly repeated minute-long quasi-static tests. Cem. Concr. Res. **82**, 36–49 (2016). https://doi.org/10.1016/j.cemconres.2015.11.007
15. Kupfer, H.: Das Verhalten des Betons unter mehrachsiger Kurzzeitbelastung unter besonderer Berücksichtigung der zweiachsigen Beanspruchung [The Behavior of Concrete under multiaxial Short Time Loading especially considering the biaxial Stress]. DAfStb Heft 229, Ernst & Sohn (1973)

16. Kuttke, P., Hellmich, C., Scheiner, S.: A principle of virtual power-based beam model reveals discontinuities in elastic support as potential sources of stress peaks in tramway rails. Acta Mech. **231**, 4641–4663 (2020). https://doi.org/10.1007/s00707-020-02776-7
17. Königsberger, M., Irfan-ul Hassan, M., Pichler, B., Hellmich, C.: Downscaling based identification of nonaging power-law creep of cement hydrates. J. Eng. Mech. **142**(12), 04016106 (2016). https://doi.org/10.1061/(ASCE)EM.1943-7889.0001169
18. Königsberger, M., Hlobil, M., Delsaute, B., Staquet, S., Hellmich, C., Pichler, B.: Hydrate failure in ITZ governs concrete strength: a micro-to-macro validated engineering mechanics model. Cem. Concr. Res. **103**, 77–94 (2018). https://doi.org/10.1016/j.cemconres.2017.10.002
19. Lackner, R., Macht, J., Hellmich, C., Mang, H.: Hybrid method for analysis of segmented shotcrete tunnel linings. J. Geotech. Geoenviron. Eng. **128** (2002). https://doi.org/10.1061/(ASCE)1090-0241(2002)128:4(298)
20. Markovitz, H.: Boltzmann and the beginnings of linear viscoelasticity. Trans. Soc. Rheol **21**(3), 381–398 (1977). https://doi.org/10.1122/1.549444
21. Neuner, M., Dummer, A., Schreter, M., Hofstetter, G., Cordes, T., Bergmeister, K.: Nonlinear time-dependent analysis of the load-bearing capacity of a single permanent shotcrete lining at the Brenner base tunnel. Struct. Eng. Int. **30**(4), 475–483 (2020). https://doi.org/10.1080/10168664.2020.1735979
22. Oreste, P.: The convergence-confinement method: roles and limits in modern geomechanical tunnel design. Am. J. Appl. Sci. **6**(4), 757–771 (2009). https://doi.org/10.3844/ajassp.2009.757.771
23. Pacher, F.: Deformationsmessungen im Versuchsstollen als Mittel zur Erforschung des Gebirgsverhaltens und zur Bemessung des Ausbaus [Measurements of Deformations in Experimental Tunnels to explore the Behavior of Rock and to Design the Lining]. Felsmechanik und Ingenieurgeologie **1**, 149–695 (1964)
24. Panet, M.: Le calcul des tunnels par la méthode convergence-confinement. Presses ENPC (1995)
25. Ruiz, M., Muttoni, A., Gambarova, P.: Relationship between nonlinear creep and cracking of concrete under uniaxial compression. J. Appl. Concr. Technol. **5**(3), 383–393 (2007). https://doi.org/10.3151/jact.5.383
26. Salençon, J.: Handbook of continuum mechanics: general concepts thermoelasticity. Springer Berlin Heidelberg (2001). https://books.google.at/books?id=MZf-CAAAQBAJ
27. Salençon, J.: Virtual Work Approach to Mechanical Modeling. John Wiley & Sons, Inc. (2018)
28. Scheiner, S., Hellmich, C.: Continuum microviscoelasticity model for aging basic creep of early-age concrete. J. Eng. Mech. (ASCE) **135**(4), 307–323 (2009). https://doi.org/10.1061/(ASCE)0733-9399(2009)135:4(307)
29. Schubert, W., Steindorfer, A.: Selective displacement monitoring during tunnel excavation. Felsbau **14**(2), 93–97 (1996)
30. Steindorfer, A., Schubert, W., Rabensteiner, K.: Problemorientierte Auswertung geotechnischer Messungen—Neue Hilfsmittel und Anwendungsbeispiele [Advanced Analysis of Geotechnical Displacement Monitoring Data: New Tools and Examples of Application]. Felsbau **13**(6), 386–390 (1995)
31. Sulem, J., Panet, M., Guenot, A.: An analytical solution for time-dependent displacements in a circular tunnel. Int. J. Rock Mech. Mining Sc. Geomech. Abstr. **24**(3), 155–164 (1987). https://doi.org/10.1016/0148-9062(87)90523-7
32. Sulem, J., Panet, M., Guenot, A.: Closure analysis in deep tunnels. Int. J. Rock Mech. Mining Sci. Geomech. Abst. **24**(3), 145–154 (1987). https://doi.org/10.1016/0148-9062(87)90522-5
33. Tamtsia, B., Beaudoin, J., Marchand, J.: The early age short-term creep of hardening cement paste: load-induced hydration effects. Cement Concr. Compos. **26**, 481–489 (2004). https://doi.org/10.1016/S0958-9465(03)00079-9
34. Touratier, M.: An efficient standard plate theory. Int. J. Eng. Sci. **29**(8), 901–916 (1991). https://doi.org/10.1016/0020-7225(91)90165-Y
35. Touratier, M.: A refined theory of laminated shallow shells. Int. J. Solids Struct. **29**(11), 1401–1415 (1992). https://doi.org/10.1016/0020-7683(92)90086-9
36. Ullah, S., Pichler, B., Hellmich, C.: Modeling Ground-Shell Contact Forces in NATM Tunneling Based on Three-Dimensional Displacement Measurements. J. Geotech. Geoenviron. Eng. **139**(3), 444–457 (2013). https://doi.org/10.1061/(ASCE)GT.1943-5606.0000791
37. Ullah, S., Pichler, B., Scheiner, S., Hellmich, C.: Shell-specific interpolation of measured 3D displacements, for micromechanics-based rapid safety assessment of shotcrete tunnels. Comput. Model. Eng. Sci. **57**(3), 279–316 (2010). https://doi.org/10.3970/cmes.2010.057.279
38. Ullah, S., Pichler, B., Scheiner, S., Hellmich, C.: Influence of shotcrete composition on load-level estimation in NATM-tunnel shells: micromechanics-based sensitivity analyses. Int. J. Numer. Anal. Meth. Geomech. **36**, 1151–1180 (2012). https://doi.org/10.1002/nag.1043
39. Wang, H., Binder, E., Mang, H., Yuan, Y., Pichler, B.: Multiscale structural analysis inspired by exceptional load cases concerning the immersed tunnel of the Hong Kong-Zhuhai-Macao Bridge. Underground Space **3**, 252–267 (2018). https://doi.org/10.1016/j.undsp.2018.02.001
40. Zhang, J.L., Vida, C., Yuan, Y., Hellmich, C., Mang, H.A., Pichler, B.: A hybrid analysis method for displacement-monitored segmented circular tunnel rings. Eng. Struct. **148**, 839–856 (2017). https://doi.org/10.1016/j.engstruct.2017.06.049